Swiss Federal Institute of Technology Lausanne

Master thesis, Department of Physics

Development of high band gap protocrystalline material for p-i-n thin film silicon solar cells

Fabio MAURIZIO

Professor: Christophe BALLIF
Supervisor: Michael STUCKELBERGER

Neuchâtel – January 2012

Institute of Microengineering IMT
Photovoltaics and thin film electronics laboratory PV-LAB

Abstract

High band gap thin film silicon solar cells are of high interest for the use as top cell in triple junctions solar cells. Protocrystalline silicon, in the transition phase between amorphous and microcrystalline silicon, is such a high band gap material.

During this project, protocrystalline intrinsic layers have been developed and optimized in p-i-n single junction solar cells by plasma-enhanced chemical vapour deposition (PECVD) in a new multi-chamber deposition system. In the first series, cells and layers were deposited with different dilutions going from silane to hydrogen flux ratios of 1:1 to 1:64. At the dilutions 1:16 and 1:32, protocrystalline material was obtained which showed amorphous characteristics only up to a certain thickness, where crystallites started to evolve.

With dilution 1:16, a second cell series has been deposited with variation of the intrinsic layer thickness. The best cells in terms of open-circuit voltage and fill factor product were obtained with an i-layer thickness of 100 nm. These cells have open-circuit voltages and fill factors up to 0.975 V and 75.8 % (0.932 V and 69.9 %) for the initial (degraded) state. These are promising values for the use of this material in top cells. However, the low current density means that the optimum i-layer thickness is probably higher for triple cell application.

Further cells have been deposited at different temperatures. These results imply that there is still room for further optimization, when current limitations of the heating system will be overcome.

Contents

1. Introduction

1.1 Current status of photovoltaic technology

The year 2011 could become an important date in the history of energy production technology especially from the political point of view. Many political decisions about the future of energy production in Europe as well as in the rest of the world are reconsidered. Sadly, the rethinking was not spontaneous, but initiated by the tragedy of Fukushima which has made the politicians and economists searching with more willingness for alternatives to nuclear power plants. In Switzerland as well as in Germany, the authorities think about totally renounce to atomic power plants. That aggravates even more the energy production problem, but at the same time opens new opportunities for people developing other energy sources.

The solar energy has a minimal production share of the total energy production and it is not expected to replace completely nuclear power plants in near future. However, the potential of photovoltaic (PV) electricity production is often underestimated. Together with other renewable energies sources (e.g. hydro electrical, wind, solar thermal, biomass and geothermal) it could provide an energy source mix which could make our society completely independent form any kind of fossil source.

The PV electricity production in the last 10 years has grown a lot (see Figure 1.1) and there is much more potential: 100 km^2 of well oriented roofs are available in Switzerland which could theoretically provide 16% (annually around 9.5 TWh) of the Swiss electricity consumption [1].

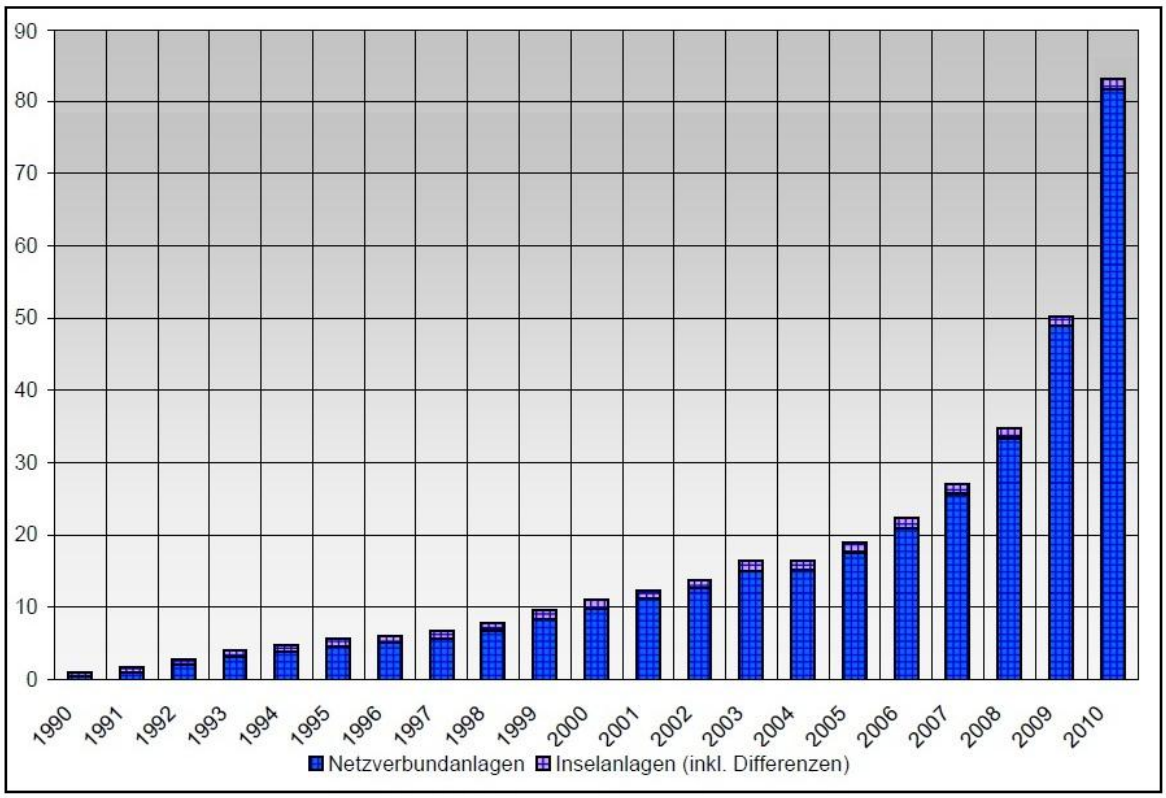

Figure 1.1: Photovoltaic electricity production in Switzerland in GWh/year (blue: grid-connected, violet: stand-alone) [2]

The vast majority of the installed PV modules use traditional crystalline wafers, but in future thin film silicon solar cells could replace and/or complement this market to a larger extent. The advantages of thin film solar cells are fewer production steps (the number is strongly reduced in comparison to the full production chain for crystalline silicon) and less material requirement than for classical crystalline silicon solar cells production. Both contribute to lower the production cost and the final $/W ratio as well as the energy payback time. Figure 1.2 shows a simplified thin film module. In particular, silicon thin film cell could contribute to the growth of the PV technology to an important share in the electricity production mix, due to the fact that silicon is not considered a rare raw material in comparison to the materials used for other thin film solar cells (see section 2.1.1). However, one of the main drawbacks of the silicon thin film cell modules is the quite low efficiency (the micromorph solar module X3-140 of Inventux has an efficiency of almost 10 % [3] and it is one of the world best modules). Therefore, a lot of research in this field is still needed.

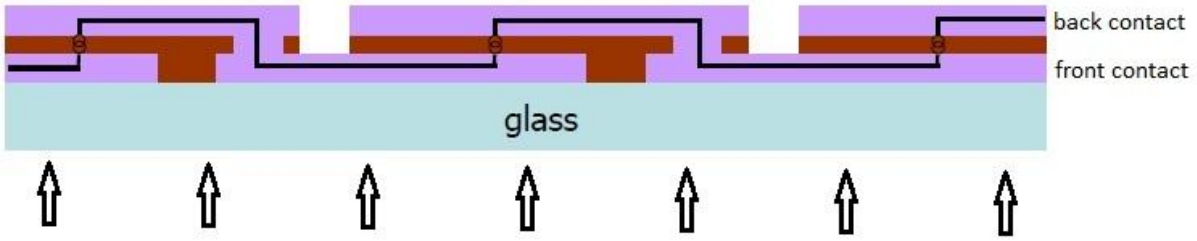

Figure 1.2: Big p-i-n cell divided into sub-cells connected in series by just three laser scribe steps after each deposition (front contact, silicon layer and back contact). Courtesy of the PV-lab.

1.2 Project motivation and outlook

The PV-lab research group is developing silicon thin film solar cells in order to improve their performance. The topic of this project is the development of the intrinsic layer of the top cell of a triple junction to improve its total efficiency. This should be reached using protocrystalline silicon which is known to have a high band gap [4], in the intrinsic layer. A higher band gap leads to a higher open-current voltage (V_{oc}) value of the topcell and thus to a better energy conversion efficiency of the high energy photons of the solar spectrum.

More concretely, the goal is to get a top cell for a triple-junction cell with a very high fill factor (FF) and V_{oc} product, because usually in triple-junction cells the current is already limited by the middle or bottom cells. It is already known from former researches that changing the hydrogen dilution during the deposition affects the crystallinity and the V_{oc} of the cells [4]. The intrinsic layer thickness and the deposition temperature influence V_{oc} and FF too. The effect of these three parameter's variation in the intrinsic layer recipes were thus analysed in order to optimize the layer properties. The doped layers were kept as identical as possible in order to avoid undesired influences coming from that.

In the theory chapter 2 the operational mode of p-i-n cells, the triple junction cell in more detail and the properties of protocrystalline silicon are explained for a better comprehension of the topic.

In chapter 3, the cell production steps as well as the measurement methods are illustrated before presenting and commenting the results in the last chapters.

2. Theoretical background

A solar cell is a semiconductor device, basically a diode, which directly converts the energy coming from the sun light radiation into electrical energy. This phenomenon is generally known as the photovoltaic effect. In the classical cells made from crystalline silicon wafers (monocrystalline or polycrystalline), the electron/hole pairs created by absorption of the photons are collected by diffusion towards the two extremities of the p-n junctions. In thin film silicon cells, the charged particles are separated and collected by drift due to the electric field in the intrinsic layer situated between the negatively doped n-side and the positively doped p-side. This is the main difference in operation principle of the thin film cells in comparison to classical cells. More details about thin film silicon cell technology will be given in the next section.

Silicon is the mostly used material in photovoltaic application even if it is a semiconductor with an indirect bandgap and has therefore a lower absorption coefficient then semiconductors with direct bandgaps such as GaAs or CdTe. To compensate the lower absorption coefficient, thick absorbers can be used like in classical silicon solar cells, or sophisticated light-trapping techniques as in thin film silicon cells.

Figure 2.1 shows the energy distribution of the photons arriving from the solar irradiance. AM1.5g spectrum means the spectral irradiance of the sun with an air mass coefficient of 1.5 atmosphere thickness which is used for the most calculations in PV research. The letter g stand for global (direct plus diffused) irradiation and the spectrum is in general normalized at 1000 W/m^2. AM0 is the spectrum before the light enters the atmosphere which can be approximated by a black body spectrum at 6000K.

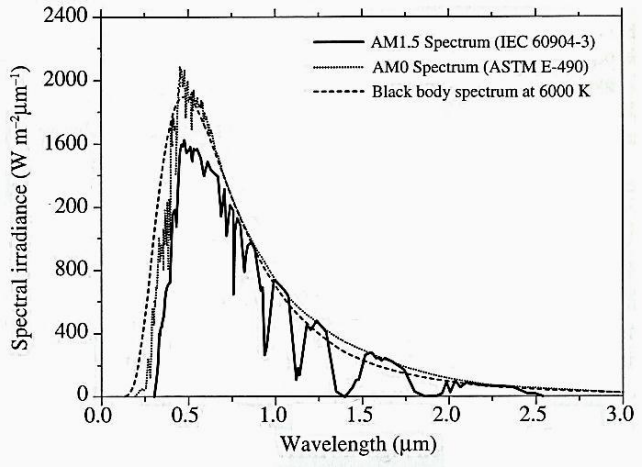

Figure 2.1: Sun spectral irradiance at the earth's surface (AM1.5) and outside the atmosphere (AM0) [5].

A very important parameter is the value of the energy bandgap (E_g). In the ideal absorption case, E_g equals to the energy of the absorbed photon

$$E_{ph} = h \cdot \nu = \frac{h \cdot c}{\lambda}$$

where h is the Planck constant, ν the wave frequency of the photon, c the speed of light and λ the wavelength of the photon. E_g is a material property and it is constant for an absorbing layer: crystalline silicon has a bandgap of about 1.1 eV and hydrogenated amorphous silcon of around 1.7 eV [5]. If $E_{ph}<E_g$, the photon energy is not sufficient to create an electron/hole pair and will be not be absorbed. If $E_{ph}>E_g$, an electron/hole pair can be created, but the difference in energy will be lost in thermalization (phonons excitations). Therefore a compromise is desired, between absorbing enough photons and not losing too much energy in thermalization. Energy bandgaps in the range between 0.8 eV and 1.5 eV [5] are best suited for single junction solar cells under AM1.5g illumination. This

first compromise already limits the theoretical conversion efficiency maximum at about 45 % [5]. The theoretical limit will be further decreased to around 30 % due to electron/hole pair collection limits and parasitic absorption.

2.1 Thin film solar cells

It was already mentioned in the introduction that one of the main advantages of thin film solar cells is their lower material requirement in production. Effectively, they have a thickness which varies between few hundred nanometers and few micrometers (see Figure 2.2). However, the efficiency of thin film cells does not reach the values of the classical cells. It is the challenge for the research and development sector to improve it. While cadmium telluride (CdTe) and copper-indium-gallium-selenide (CIGS) thin film cells already show top efficiency values of 16.7% and 20.3 %, respectively, on laboratory scale, the best silicon thin film cells have a maximum of 12.5% so far. (See figure with record solar cells in the appendix [6])

However, the fact that thin film silicon solar cells are based on abundant and nontoxic materials (Si, B, P, C, H, O and Sn or Zn) makes this technology very promising for mass production. Indium or Tellurium could become rare and expensive with increased use and cells containing cadmium could cause problems due to acceptance or environmental reasons [5].

2.1.1 p-i-n- single junction solar cells

The p-i-n cells are deposited on glass because the light has to pass through it and the first layer to deposit is the front contact. Figure 2.2 shows the exact layer succession in a p-i-n cell. p-, i- and n-layer stand for positively doped, intrinsic and negative doped silicon layers. The front contact has to be transparent and conductive. Therefore, ZnO or SnO_2 are mostly used. Due to their properties they are called transparent conducting oxides (TCO). Often not smooth, but pyramidal shaped TCOs are used to get a rough interface between the TCO and the silicon layers which diffuses the light. That increases the path of the photons within the absorbing layer and compensates partially the fact that the layer is too thin. The p-layer contains boron atoms as positive dopants as well as carbon which increases the bandgap and lowers parasitic absorption losses in the p-layer. Therefore it is also called window layer. This characteristic is desired because the electron/whole pairs would probably recombine in the p-layer. So the photons are preferred to be transmitted to the intrinsic layer where they are mainly absorbed and the electron/hole pairs well collected. On one side, the i-layer has to be thin in order to have an electrical field which is strong enough to collect the charged particles at the two extremities, but on the other thick enough for an efficient absorption. This is called the optical/electrical trade-off. The n-layer is usually doped by phosphor atoms and is a window layer too. Hence non-absorbed photons are preferred to be transmitted: Depending if it is followed by another cell (in multi junction cells) or has a reflective metal (in single junction cells), the non-absorbed photons are transmitted to the next cell or reflected again to the i-layer.

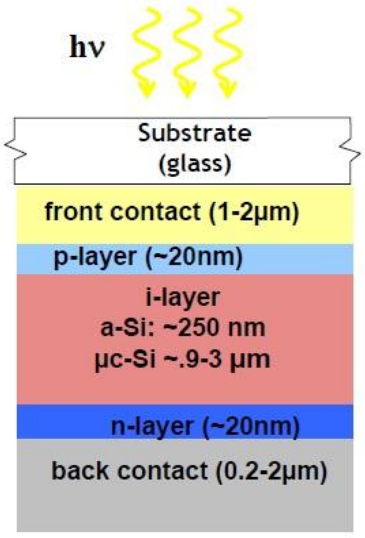

Figure 2.2: Layers description for a p-i-n cell. Courtesy of the PV-lab.

Similar to the classical p-n cells the main operational principle of a p-i-n cell consists of two steps: The first step, in the extraction of electrical energy from a solar cell, is the generation of free electrons

and holes due to the photovoltaic effect. As second step, the created free electrons and holes have to be separated and collected. This is possible due to the present electrical field which accelerates the negatively charged electrons in one direction and the positive charged holes in the opposite one (see Figure 2.3a). The electrical field is present thanks to the diode-like p-n structure of the solar cell. In contrast to the p-n type diode, where the electric field is limited to the depletion layer, in a p-i-n type diode the electric field extends over the whole intrinsic layer. The separation as well as the collection of the charged particle is drift driven, contrarily to the collection in a p-n cell which is diffusion driven. The stronger the electric field, the more efficient is the charge collection.

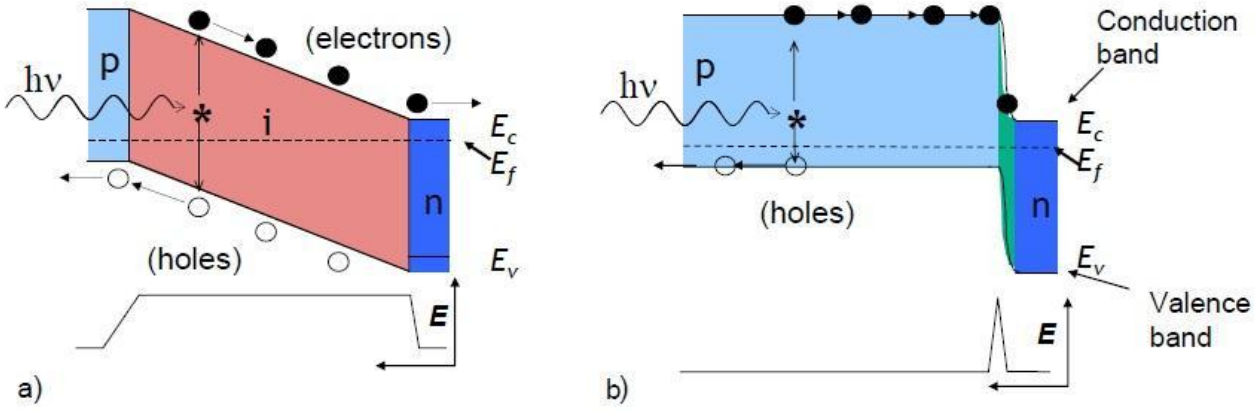

Figure 2.3: The p-i-n thin film solar cell (a) is drift driven, while the classical crystalline p-n cell (b) is diffusion driven. Courtesy of the PV-lab.

The electrical behaviour of an amorphous silicon thin film solar cell can be approached by an equivalent circuit (see Figure 2.4): The measured current consists basically of a diode term, a term for the photo current under illumination (because of the photo-generated charge particles) and a term due to recombination losses in the cell. The parallel and series resistances should ideally tend to infinity and to 0, respectively. This is a model with a non-trivial assumption, which could indeed be proven being quite precise by experimental measures. To the model for classical solar cells the component representing J_{rec} (recombination current density) is added, because the dangling bonds present in amorphous silicon act as recombination centres if they are not well "passivated". A possible way to describe this term is using the following formula [7]:

$$J_{rec} = J_{ph} \cdot \frac{d^2}{(\mu \cdot \tau)_{eff} \cdot [V_{bi} - (V - I \cdot R_s)]}$$

J_{ph} is the photo generated current density, d the thickness of the i-layer, $(\mu \cdot \tau)_{eff}$ the effective driftlength which is the product of the mobility (μ) and the life or capture time (τ) of the charged particles, V and V_{bi} the voltage and bias voltage respectively, I the current and R_s the resistance in series.

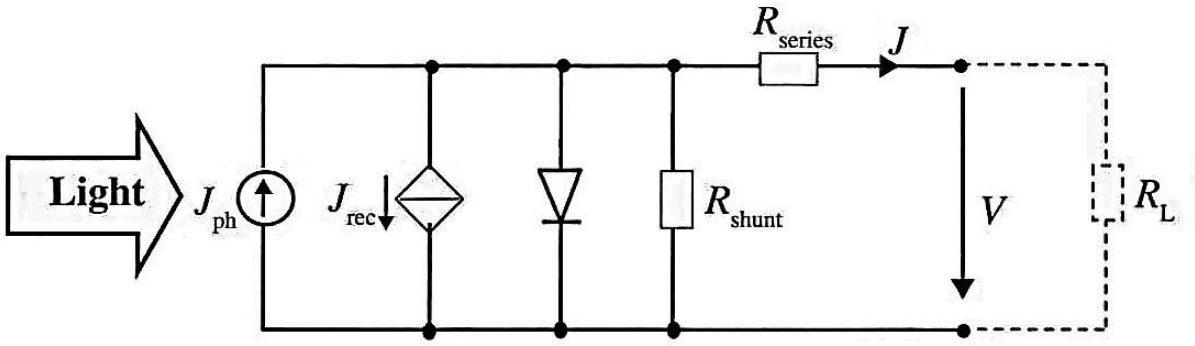

Figure 2.4: Circuit which corresponds to a thin film amorphous silicon solar cell [5].

Figure 2.5 shows the maximum power point (MMP) at which the solar cell delivers the maximum power to a load as the name already says. I and V can be linked to each other due to the Ohm's law by the load resistance R_L:

$$V = R_L \cdot I$$

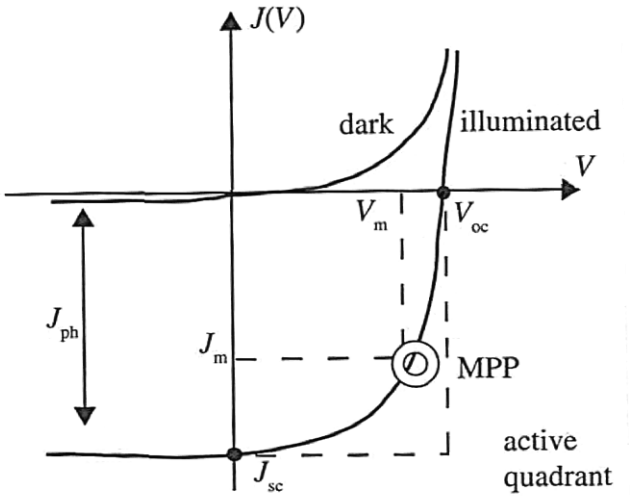

Figure 2.5: Current superposition model. Edited figure from [5]

The current density and voltage corresponding to the MPP are called J_{mpp} or J_m and V_{mpp} or V_m. The short-circuit current density (J_{sc}) is the current density when no voltage is applied. It depends directly on the quantity of absorbed photons. The thicker the absorbing layer, the more photons are absorbed. There is however a limit which mainly depends on the bandgap of the semiconductor and on the spectral distribution of the light. The open-circuit voltage (V_{oc}) is the voltage where there is no current. A higher energy bandgap usually leads to a higher V_{oc}.

From these values the fill factor (FF) which is defined as

$$FF = \frac{J_{mpp} \cdot V_{mpp}}{J_{sc} \cdot V_{oc}}$$

can be calculated. It is the ratio of the maximum output power density of the solar cell to the product of J_{sc} and V_{oc}. Geometrically it corresponds to the ratio between the surfaces of the two dashed rectangles displayed in Figure 2.5. For amorphous silicon thin film solar cells of good quality the FF values should be between 0.75 % (initial state) and 65 % (in the degraded state) [5].

2.1.2 Multi-junction solar cells

It was explained before that the theoretical efficiency potential of single junction solar cells is strongly limited. The theoretical maximum is less than 30% even for the best suited material with a bandgap of around 1.4 eV [5].

For this reason, new solutions are developed in order to increase the potential efficiency. One option is to build tandem or multi-junction solar cells. These are composed of several cells deposited one on the other, ideally each with a different energy band gap. For example, the triple junction solar cell has a high band gap top cell which efficiently absorbs just the high-energy part of the solar spectrum. The rest of the light is transmitted and the middle energy part is absorbed by the middle cell, while the remaining low energy part is finally absorbed by the bottom cell. This method allows absorbing a lot of photons using the larger part of their energy and thus increases the potential total cell efficiency. In Figure 2.6, the high, middle and low energy part of the solar spectrum are represented by the blue, green and red colour respectively. The bandgap combination of 1.1 eV/ 1.75 eV in a tandem cell would raise the maximal theoretical efficiency to around 39% [5]; in triple 49 % could be reached for the ideal combination and for a theoretical infinite number of cells 68% would be possible [8].

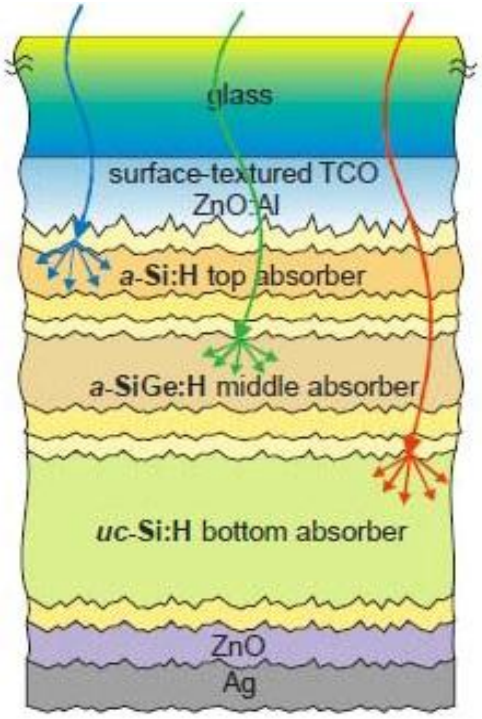

Figure 2.6: Example of a triple-junction thin film solar cell [18]

However, new technologies are always accompanied by new challenges. At the cell junctions, the recombination efficiency has to be optimized and due to the fact that the cells are connected in series, the different cells have to produce the same current, because this would be limited in any case by the smallest one. These are some of the challenges in the multi-junction research field.

2.2 Protocrystalline silicon

Silicon can appear in several forms. The best known is probably crystalline silicon. The material applied for the classical PV cells is either multi- or polycrystalline silicon with grains of a magnitude from several millimetres to some centimetres or monocrystalline silicon which is a homogenous crystalline material. In thin film technology there is another form of crystalline silicon called microcrystalline because of the grain dimension in the micrometre range or even less.

In addition, there is the amorphous form of silicon where all crystalline symmetries are broken. Amorphous silicon shows in general a very high dangling bond density. For this reason, hydrogen is usually added during the deposition process. The hydrogen atoms bind to the dangling bonds and passivate so the material, what allows the building of semiconductors devices. The passivation lowers the defect density by a couple orders of magnitude.

A crystal phase diagram of hydrogenated silicon (Si:H) is obtained by varying the hydrogen dilution R=[H2]/[SiH4] during the PECVD deposition (see Figure 2.7). At very low deposition dilution, the material is completely amorphous while at very high dilution it is microcrystalline. In the transition regime, the transition boundary depends from the bulk layer thickness (d_b) too. “Protocrystalline Si:H is

the term first applied by Koh et al. [9] to describe a-Si:H optimized for devices by deposition at the maximum possible R value that can be sustained without crossing the a-(a+μc) transition boundary for the desired bulk layer thickness." [10] It has been shown that producing cells with the intrinsic layer in this regime slightly increases the V_{oc} of the cell [9], before it decreases due to the lower energy bandgap of the crystalline material when the dilution is increased beyond the transition boundary.

Hydrogen dilution and bulk layer thickness are thus important factors for the nucleation density of crystallites in the deposited layer and in high efficiency solar cells.

It was also observed that the substrate on which the layer is deposited can cause a shift of the boundary line in the crystal phase diagram [11]. This is thus another parameter which has to be considered.

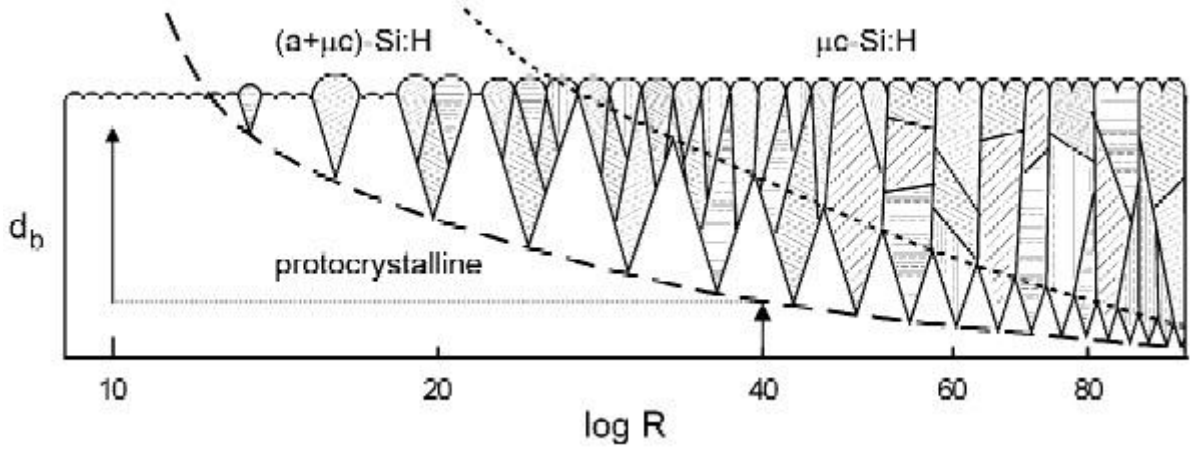

Figure 2.7: Transition region between microcrystalline and amorphous silicon with the protocrystalline phase [10].

A characteristic phenomenon of amorphous or protocrystalline silicon is the reversible light-induced degradation process that is called Staebler-Wronski effect [12]. This occurs when amorphous cells are exposed to light or an electric current is injected into them. The weaker bonds within the amorphous silicon network are broken and so new dangling bonds are created which act as recombination centres. The larger recombination current density makes the efficiency of the cells decrease, especially due to a fill factor reduction [7]. Because of that it is always necessary to repeat the measurements of the cells properties after several hundred hours of light soaking. However, by annealing the solar cells at temperatures around 150-250°C for a time varying from some minutes to a few hours, depending on the temperature, the effect can be reversed [5].

3. Experimental methods

In this chapter, the processing steps and the measurement carried out during the project are presented.

3.1 Cell processing steps

Starting from the glass substrate to the ready-to-measure cell there are several steps which have to be carried out carefully to get a working solar cell. These are presented in the following subsections.

3.1.1 Substrate preparation

The substrate of the cells and layers are glass plates with a dimension of 4.1 cm x 8.2 cm and a thickness of 0.5 mm. These are prepared and cleaned in the clean room in order to avoid any kind of initial contamination. When deposing a silicon layer, they are directly loaded into the deposition system, while for the cells the front contact deposition is necessary first.

3.1.2 Front- and back contact deposition

Glass substrates with a front contact deposited on it are ready to use in the PV-lab for cell depositions. However, there is no difference in the processing mode in comparison to the back contact deposition. Both are low pressure chemical vapour depositions (LP-CVD). Thereby, a vapour-gas mixture of water, diethyl-zinc (DEZ) and diborane is injected into the deposition chamber. By an exothermal process, a conductive ZnO-layer of a thickness between 1 to 5 µm depending on the deposition time is deposited as TCO. The boron atoms are the dopants which make the ZnO conductive. To get a similar conductivity, the recipe for thinner layers has a higher diborane flux than the recipe for thicker layers.

As front contact Z1, Z2 and Z5 substrates are prepared. The numbers after the letter Z are the approximate layer thicknesses in micrometres. B52 is a variant of the Z5 often used as a back contact. For the B52 the Z5 recipe is used, but the deposition time is just the half.

3.1.3 Surface treatment

The substrates with the deposited ZnO can be exposed to an argon plasma treatment in the Oxford machine. This surface treatment smoothens the pyramids of the ZnO layer and turns the initial “V” shape into rather “U” shape (see Figure 3.1).

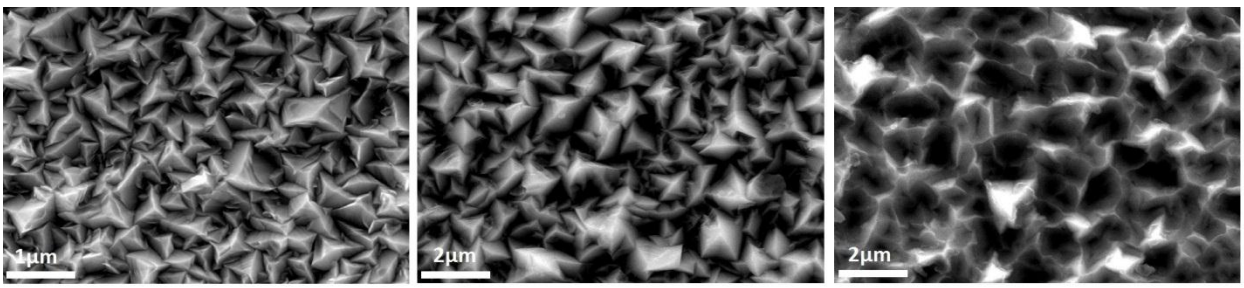

Figure 3.1: SEM micrographs of different front-contacts. On the left an untreated Z2, in the middle an untreated Z5 and on the right a Z5 after 80 min surface treatment. Source: [13]

Although the pyramidal shape of the ZnO has a positive effect on the photon absorption due to the light scattering (see trapping effect [14] improving the current in section 2.1.1), it is necessary to smoothen the pyramids in order to limit shunt probability.

For this project, cells were deposited on four different substrates: three Z2 substrates with an argon treatment of 40 min, 15 min and 4 min respectively and an untreated Z1 substrate. Smooth substrates permit to determine the optimum electrical performance achievable with the developed p-i-n layers, while performances on increasing roughness of the substrate texture allow assessing the resilience of the developed processes to the substrate roughness.

3.1.4 Deposition (PECVD)

During the plasma-enhanced chemical vapour deposition (PECVD), plasmas are used in the CVD reactors to "activate" and partially decompose the precursor gas molecules (silane and hydrogen for the intrinsic layers; for the p- and n-layer, Trimethylborane (TMB or $B(CH_3)_3$) and phosphine (PH_3) are added as dopants. The plasmas are generated by applying an AC voltage between the two parallel electrodes in the radio frequency range and usually a spark ignites them. The deposition takes place under low pressure conditions and at a temperature lower than thermal CVD [15] similar to the temperature during the ZnO LPCVD. However in contrast to the LPCVD, in PECVD the plasma is needed to overcome the large potential barrier when dissociating the silane and hydrogen molecules.

Cell and layer depositions and optimisations represent the main part of the project and all the thin film silicon depositions were accomplished in the new deposition system which is called Octopus, fabricated by Indeotec, spin-off company of the PV-Lab. The machine is still under the development, so the users contributes to it with feedbacks and suggests.

Octopus machine

As the name tells us, this thin film deposition machine has place for eight different chambers including the load lock. Currently, 5 deposition chambers are in use: In chamber A, amorphous intrinsic silicon layers are deposited, while the chamber B is mostly used for microcrystalline intrinsic silicon layers. In the chambers C and D, the doped layers p-type and n-type, respectively, are deposited. In chamber E intrinsic silicon layers are done under high pressure condition. The clear separation of intrinsic and doped layer's deposition should avoid eventual contaminations of the layers or the chambers. During preheating, impurities which came on the substrate-holder when loading could effectively contaminate the environment by evaporation. Especially the chambers used for intrinsic layer depositions could be easily contaminated by dopants. Because of that the substrate-holders were always preheated either in chamber C or D before deposition. In addition in the chambers used for intrinsic silicon depositions, doped gases that remained in the gas line from previous depositions should not be injected. For this reason a purge of the gas lines was carried out after every doped layer deposition. Besides that, an intrinsic layer was deposited on the substrate-holders to have reproducibly uncontaminated surfaces for the next deposition.

Figure 3.2: Picture of Octopus PECVD system. The glass door of the load lock chamber with some substrate-holder inside is clearly visible together with the chamber A in the foreground.

In comparison to other deposition systems, the Octopus has the advantage that several substrate-holders (in the load lock there is space for up to 10) can be loaded simultaneously and all the mechanical transfer motions as well as the gas opening or pumping valves and ignite commands can be controlled automatically by the computer. The further goal is to be able to load the substrates and launch the deposition recipes of several cells without the need of the user's presence during all the deposition time.

The deposition of the majority of the cells for this project was done in chamber C, A and D for the p-, i and n-layers respectively. At the beginning of the project, the intrinsic layer of a series of cells was deposited in chamber B. That did however not bring good results, so the intrinsic layer deposition was continued in chamber A. Later, the p-layer was deposited in chamber D due to hardware problems in chamber C. Typical deposition parameters of each chamber are shown in Table 3.1.

	Chamber A	Chamber B	Chamber C	Chamber D	Chamber E
Frequency [MHz]	13.56	81.36	40.68	40.68	13.56
Power density [W/cm^2]	0.022	0.090	0.067	0.090	
Pressure [mbar]	1.0	0.7	0.7	0.7	
Temperature [°C]	200	180	200	200	200

Table 3.1: Mostly used parameters for the silicon layer depositions. In chamber E no depositions, but just plasma tests were carried out for this project.

It is known that lowering the deposition temperature give rise to a semiconducting material with a higher bandgap [16].

3.1.5 Cell structuring

The structuring of the cell is necessary for doing the measures afterwards. In the PV-Lab two methods are commonly used:

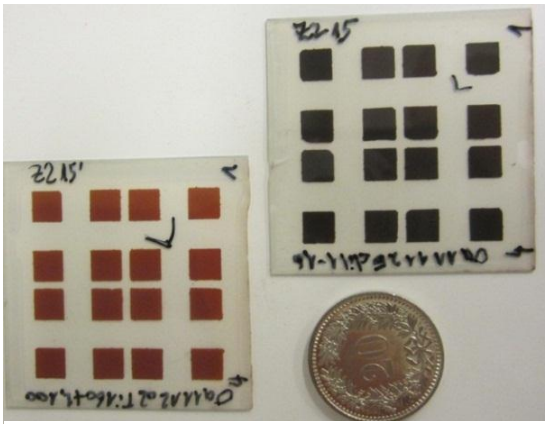

Figure 3.3: Cells structured with the split off method.

The lift off process consists in painting with an organic felt pen the surface where the silicon layer should disappear before depositing the back contact. When the deposition is done, the cells are immersed in acetone and the back contact over the painted region gets so dismantled. In this region the silicon appears at the surface again. At this point the cells are put in the Ion Projection Lithography (IPL) machine which etches the silicon layer with a SF_6-plasma till the front contact layer is reached. The back contact layer protects the silicon from the etching process where the final 16 subcells shall remain and so the desired structure as shown in Figure 3.3 is obtained.

The second way to obtain the desired 16 subcells-structure is to use the laser scribe machine. This system is more convenient to use in production lines but at the moment in the lab the first described process is preferred. The cells with the laser scribe structure usually show more shunt problems in the lab. Laser scribing is actually very sensitive if different materials and thicknesses are used. In a research laboratory where a lot of tests are done, it is thus hard to optimize the scribing for each type of cell.

3.2 Measurements of cell properties

After the deposition, the measurement of the cell performance and the layers properties is essential to get the results. First the two electrical measures for the cell are presented and then the various layer analysing techniques are explained.

3.2.1 IV measurement

The IV (current/voltage) curve is measured under illumination at conditions near the standard test conditions, STC (25°C, AM1.5g). The solar simulator works with a combination between a xenon lamp and three halogen lamps. The cell is put into a sample holder which has a double pair of pressure pins for each subcell for 4-point measurements. One pair measures the voltage, the other the current independently each to the other. In this way undesired voltage offsets due to ohmic and contact resistances are avoided. A fan prevents the cells from overheating when illuminated. The 16 subcells are successively measured from -1.2 V to 1 or 1.1 V in 10 mV steps. The measure for each subcell is repeated twice, first at nominal intensity of 1000 W/m^2 and the second time with a filter that lowers the illumination intensity at 0.4 %. These low illumination results are useful to detect the presence of shunts.

From the IV curve, the V_{oc}, the FF and the short-circuit resistance R_{sc} (good indicator for shunts) from the cell are determined as well as the J_{sc}. The efficiency of the cell can be calculated using the following formula:

$$Eff = \frac{P_{out}}{P_{in}} = \frac{FF \cdot V_{oc} \cdot J_{sc}}{P_{in}}$$

The P stands for power density, P_{in} corresponding to the 1000 W/m^2 of the solar simulator. To calculate the current density of the subcell, its area is needed that has a size of around 0.25 cm^2, but can vary considerably from subcell to subcell due to the manual structuring method explained in section 3.1.5. So the more precise current density measure from the EQE measurement is preferred (see next subsection).

3.2.2 EQE measurement

The external quantum efficiency (EQE) is the ratio of collected electron/hole pairs to the number of incoming photons. An EQE of 1 or 100 % means that for each incoming photon an electron/hole-pair is created and collected. For the EQE measurement a xenon lamp is used as light source together with a variable grating which creates the different chromaticity. Before reaching the monochromator, the light beam goes through a chopper. The monochromatic light beam is than split into two parts. The first part illuminates a reference cell while the second part of the beam is focused on a subcell of the sample which is fixed on a sample-holder from behind with a white plate which acts as holder and backreflector. Two manually placed pressure pins connect the contacts to the measurements setup. The sample is illuminated by an external bias light to approximately simulate standard test conditions.

For the experiments done in this project, EQE was measured from 370 nm to 810 nm wavelength in 10 nm steps. This absorption spectrum of amorphous cells is limited by the energy bandgap from one side and by the absorbtion of the TCO in the UV-range from the other one. For each wavelength the current is measured and with a lock-in amplifier the desired chopper frequency is filtered out to get

just the signal coming from the monochromatic beam. Therefrom the EQE curve of the cell is developed. The measurement is carried out first with no applied bias voltage (V_{bias}) and a second time with a V_{bias} = -1 V. The difference between the two curves provides information about the charge collection within the cell.

By integration of the EQE curve, it is possible to calculate the total short-circuit current density of the cell with the following formula:

$$J_{sc}(V_{bias}) = \int_{\lambda_{min}}^{\lambda_{max}} SR(V_{bias}, \lambda) \cdot \phi_{AM1.5}(\lambda) \cdot d\lambda$$

with the spectral response $SR(V_{bias}, \lambda) = EQE(V_{bias}, \lambda) \cdot \frac{q}{E(\lambda)}$

$\phi_{AM1.5}(\lambda)$ is the solar spectrum at earth's surface illustrated in Figure 2.1, λ is the wavelength, E(λ) the energy corresponding to the wavelength and q the elementary charge. The final efficiency of the cell is calculated with this value of the current density because the size of the beam spot is well known and it completely fits in all the measured subcells.

In most cases, only the best subcell (considering the IV results) of each cell sample was measured.

3.3 Measurements of the layer properties

To improve the performances of a cell, it is important to analyse and to understand the properties of the single layers. For this reason, some intrinsic layers were deposited on glass substrates and on monocrystalline silicon wafers for the FTIR measurements. The measurements described in the following subsections were carried out.

3.3.1 Height profiler

The height profiler is used to measure the thickness of a layer. For this scope, the silicon layer has first to be removed locally with the IPL machine which etches the area where there is no felt pen painting. The sample is than put in acetone such that there are sharp boarders between the silicon layer's region and the part where the glass comes on surface.

A diamond-tipped stylus whose deflection is detected by an optical beam is than placed close to a step and with a constant force applied on it moved over the step at low speed. Following parameters were used: force of 20 µN, speed at 30 µm/s and path length of 400 µm. The difference in altitude displayed corresponds to the thickness of the sample's layer. Several measurements were applied for each sample in order to check the measure accuracy and an eventual layer thickness inhomogeneity.

The determination of the layers thickness was used to calculate the deposition rates.

3.3.2 Raman crystallinity factor

The Raman crystallinity factor tells the ratio of crystalline and amorphous silicon. To measure it, a green argon laser with a wavelength of 514 nm is used in combination with a commercial spectrometer. The focused laser beam arrives perpendicularly on the layer and its reflection goes back through the objective to a grating where a CCD camera performs a measurement of the spectrum. The measure can be repeated several times and the average spectrum is analysed in the range between 400 cm^{-1} and 550 cm^{-1}. There are effectively three possible peaks with maxima at 480, 510 and 520 cm^{-1} which can be fitted by the superposition of three Gaussian curves. The proportion between the areas of these three curves represents the crystallinity factor according to the following formula:

$$\Phi_{crist} = \frac{I_{crist}}{I_{tot}} = \frac{I_{510} + I_{520}}{I_{480+}\ I_{510} + I_{520}}$$

The first peak at 480 cm^{-1} represents the amount of amorphous silicon in the sample, while the second and the third represent the quantity of microcrystalline and crystalline silicon.

In dependence on which side of the sample it is measured (layer or glass side) the laser beam power has to be modified in order to have a sufficiently large reflected signal. The system measures the surface up to a depth that depends on the wavelength of the laser and the absorption properties of the layer. With the green argon laser and the silicon thin film layer the depth corresponds to around 100 nm.

3.3.3 Ellipsometry

Ellipsometry measurements are carried out to get the energy bandgap of the layer which is analysed. The sample is put on a substrate holder. The polychromatic light with elliptical polarization is reflected by the sample at the incident angle (70° in this case). Depending on the polarization and the wavelength the light beam is differently absorbed or reflected. Each wavelength is then analysed separately from 0.6 to 6 eV. To determine the bandgap energy, the a-Si:H material was modelled with a Tauc-Lorentz oscillator. (The modelling of these measurements was carried out by M. Stuckelberger)

At the same time, other parameters (e.g. layer thickness) were determined from these measurements too. However, it is not the goal of this project to deepen this particular and complex measurement field.

3.3.4 TEM

TEM which is the abbreviation for transmission electron microscopy is a microscopy technique that uses a beam of electrons to analyse the specimen. This has to be very thin, because the electrons need to be transmitted through the specimen and the interaction between the electron and the material give than rise to the desired figure. The resolution is significantly higher than the one of light microscopes and it is limited by the de Broglie wavelength of electrons.

The TEM imaging was carried out at the EPFL by D. Alexander.

3.3.5 FTIR

Fourier transform infrared spectroscopy is a measurement technique which is used to get the infrared absorption spectrum of a sample. Therefrom, the chemical structure of the material can be interpreted.

In contrast to the dispersive spectroscopy technique where a monochromatic light beam is shined at the sample, in FTIR a beam containing a distribution of frequencies is used. An interferometer, which contains a certain configuration of mirrors, whose positions can be varied, allows measuring the dependence of the absorption on the mirror position. By Fourier transform the desired absorption graph is then computed.

To analyse an amorphous layer, this was deposited on a monocrystalline wafer. The measured absorption curve of the layer deposited on the wafer is compared with a reference wafer. Their difference reveals chemical properties of the analysed layer.

In this project the absorption range between 1800 cm^{-1} and 2200 cm^{-1} was analysed to know the ratio between silicon atoms having just one bond with an hydrogen atom and silicon atoms having two or three hydrogen atoms bonded. The first kind of bindings shows a peak at 2000 cm^{-1} while multihydrides have a peak at 2090 cm^{-1}. Their relative quantities are represented by the following ratio:

$$R = \frac{I_{2090}}{I_{2000} + I_{2090}}$$

I_{2090} and I_{2000} are the integrals of the fitted Gauss curves with their corresponding peaks at 2090 $cm^{-}1$ and 2000 cm^{-1}. R is also called microstructure factor of amorphous silicon. A lower value means typically a better quality of the material. The fitting and calculation were carried out by M. Stuckelberger.

3.4 Light soaking

All produced cells need to be measured a second time after the degradation time due to the light-induced degradation effect explained in section 2.2. This means that the cells are put under a solar simulator for 1000 hours at AM1.5g spectral irradiation, at 50°C for simulating the real conditions when they are heated by several hours sun irradiation. There is a not negligible difference in efficiency between the initial and the degraded or stabilized state of the cells.

4. Results and discussions

During the project, 40 cell- and 23 layer-depositions were carried out. Each cell deposition generated four cells with different properties due to the four different front contacts used.

At the beginning, some plasma condition tests were done in order to know the working conditions and limits of the different chambers. The first dilution series with the intrinsic layer done in chamber B did not produce good results so all further intrinsic layers were deposited in chamber A.

For the hydrogen dilution ratios a binary logarithmic scale was mostly used (points 1, 2, 4, 8 and so on). In the plots just the best subcells of each cell is displayed (the one with the highest V_{oc}·FF product) in order to have well reproducible and interpretable diagrams.

4.1 Plasma conditions

The plasma condition tests were carried out starting with the parameter listed in Table 3.1. According to the type of test, one parameter was then varied.

4.1.1 Paschen curves

In the three chambers A, B and E plasma ignition and stabilization tests were carried out. The minimal ignite power density was searched starting from very low power and increasing it stepwise until it was possible to ignite the plasma. This procedure was repeated for different pressures. Each time the plasma was on, the chamber was evacuated in order to prevent ionized gas molecules or atoms to remain in the chamber and favour the next plasma ignition. The gas flux was composed of 5 sccm silane and 80 sccm hydrogen for all chambers, but the three chambers have different plasma excitation frequencies (13.56 MHz chambers A and E, 81.36 MHz chamber B).

The paschen curve describes this breakdown behaviour in plasma conditions, usually plotting the chamber pressure times the electrode's distance versus the breakdown voltage. It has a central minimum: By lowering the pressure starting from the minimum there is a steep increase of the ignition power needed; going towards higher pressure the increase is smoother. This trend is visible in Figure 4.1.

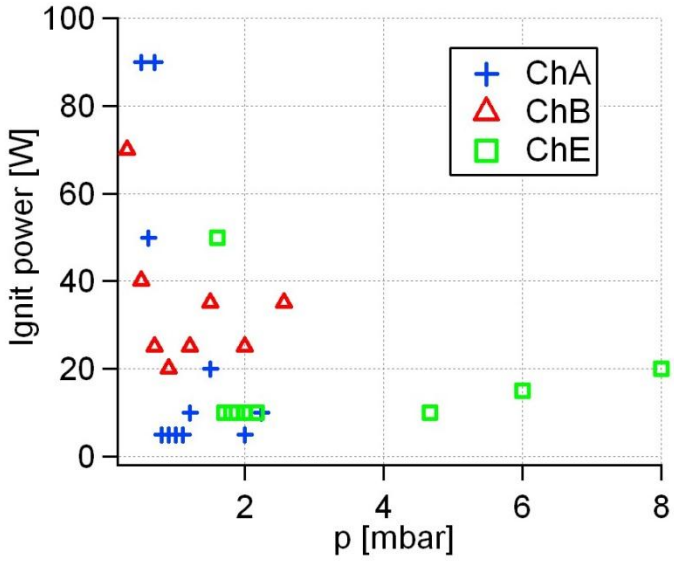

Figure 4.1: Experimental data of the plasma condition tests. At low pressure the power needed to ignite the plasma is increasing quickly to high values.

For chambers A and B it was not possible to further increase the pressure, so the ignite power increase to the higher pressure side is not noticeable. In the chamber B plasma ignitions were possible at lower pressure than in the other two chambers, because of the higher excitation frequency used in this chamber. To notice is also the higher minimum of the ignition power in the chamber B, which forced depositions at higher power density in this chamber.

4.1.2 Temperature curves

A stable temperature in the deposition chamber was difficult to maintain in some deposition processes. Especially for longer deposition with high fluxes the temperature decreased considerably. A new heating system has been installed after this project which should solve this problem for further depositions. However, the non-stable temperature profile was one of the strong system limitations during this master thesis work for the synthesis of high quality amorphous silicon material.

In Figure 4.2, the temperature trend during a long deposition with high fluxes is displayed. This might be the most extreme temperature difference between set value and real value during this project. Already at plasma ignition the difference is higher than 10°C. This happened because there were some ignition difficulties and so the gas flux already started several minutes before the beginning of the deposition. During this ignition phase the fluxes were also changed from the planned 2.5 sccm silane and 80 sccm hydrogen to 5 sccm silane and 160 sccm hydrogen.

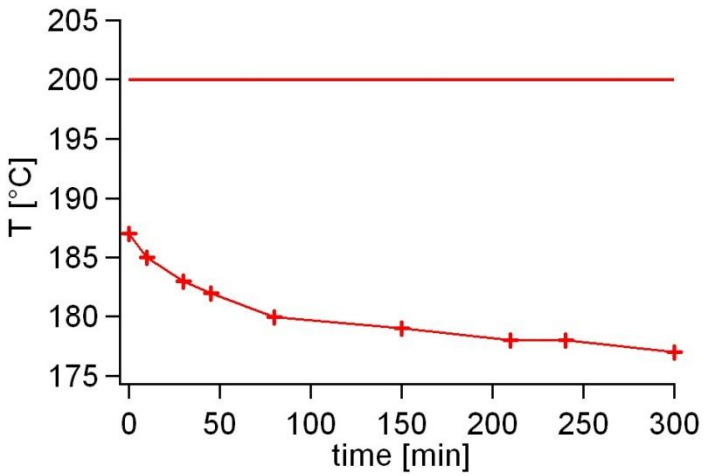

Figure 4.2: Temperature trend during the deposition of the layer Oa111118dil1-32 in chamber A. The red straight curve shows the set value at 200°C.

So when considering the results in the next sections, it is important to remember that usually the real temperature was lower than the set one. This can effectively influence in a decisive way the results. However, even if there is a systematic error due to this, the comparison within the series is still possible, because all samples were deposited under similar conditions.

4.2 Properties of the intrinsic layer

As mentioned before, the intrinsic layer was first deposited in the chamber B. However, the corresponding cells did not give satisfactory results. Their fill factors were quite low and most cells tended to be shunted: For example the best FF obtained for a subcell of 16 dilution ratio was 60.6 %, while 71.7 % were obtained for later depositions in chamber A for that dilution. In general, the best cells FF had values between 50 % and 70 % for the series deposited in chamber B. With high probability, the bad quality of these cells was a direct consequence of the bad quality of the intrinsic layer, because the p- and the n-layer recipes were those of standard cells that worked well and the tests during this

work were just focused on the intrinsic layer. Probably, the higher deposition rates in chamber B (see Figure 4.3) are responsible for a higher density of defects in the intrinsic layer. This could explain the final bad quality of the cells.

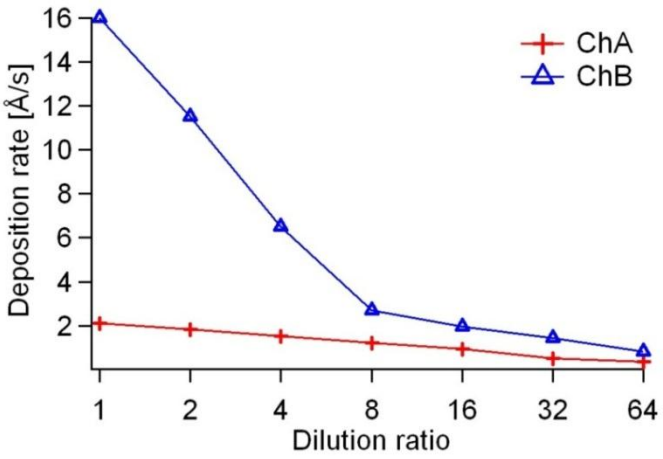

Figure 4.3: Deposition rates of the intrinsic layer as a function of their hydrogen dilution for the chambers A and B.

Because of this initial problem the study was continued with the intrinsic layer deposition in the chamber A which has the lower plasma excitation frequency of 13.56 MHz, instead of the 81.36 MHz of the chamber B. This [17] and the different power densities during the deposition are the main reasons for the different deposition rates.

For more detailed analyses of the intrinsic layers properties the Raman crystallinity and the ellipsometry measurements are presented. The FTIR measurements did not give satisfactory results.

4.2.1 Raman crystallinity

Each deposited layer was measured from both sides: the deposition or layer side and the glass side. As it was expected, with increasing hydrogen content, the amorphous silicon becomes more and more microcrystalline (see Figure 4.4). The dependence on the thickness of the layer is also apparent: the “layer side curve” increase starts at lower dilutions. This confirms the curve in the crystal phase diagram of Figure 2.7. The layer with dilution 16 is expected to be protocrystalline, as it is still amorphous on the glass side, but already shows a crystalline fraction on the layer side. This is the first indicator for a possible good cell with an intrinsic layer with a flux dilution ratio of 16.

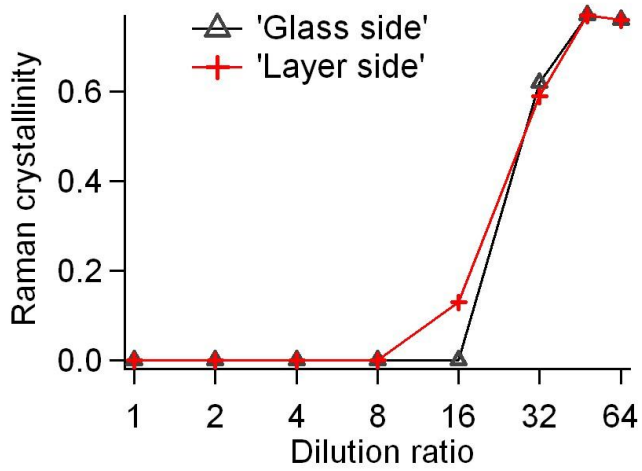

Figure 4.4: The transition from the amorphous phase to the microcrystalline phase is clearly visible between the dilution ratio of 16 and 32. At the dilution ratio of 16 the protocrystalline phase is most probably reached.

Not all layers had the same layer thickness (they vary from 90 to 220 nm), so some points could be slightly shifted if the analysis of layers with the same thickness was repeated. However, the general trend is already well visible.

4.2.2 Energy band gap

From the ellipsometry measurements the energy bandgap values of the amorphous phase are calculated (see figure Figure 4.5). Until the dilution 16 a model was used which just considers amorphous materials, because, as it was shown before, till to this dilution the material is almost completely amorphous. For the other dilutions another model, considering the crystalline content too, was applied.

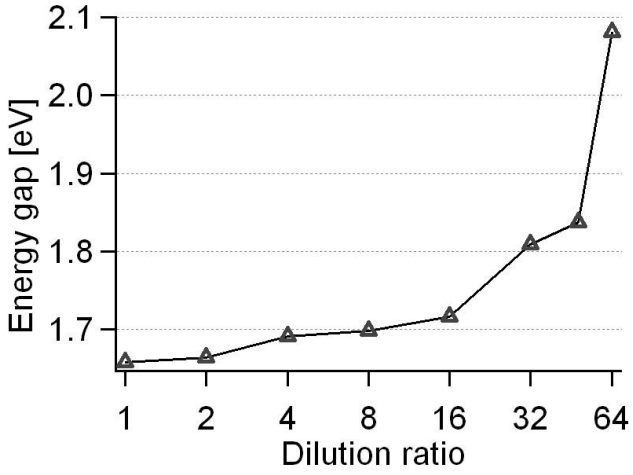

Figure 4.5: Energy bandgap increase of the amorphous silicon due to higher dilutions. Important to remember is that at dilutions above 32 the silicon is mostly microcrystalline.

The graph shows the expected increase of the energy band gap of the amorphous part of silicon when the dilution ratio is increased [16]. However, it was shown before that at dilutions above 32, the amorphous content in the silicon layer is decreasing. The V_{oc} is proportionally correlated to the E_g.

4.2.3 Microstructure factor

From the FTIR measurements the microstructure factor R of the layers was analysed. However there were some difficulties due to the layers thinness (the signal to noise ratio was too low) and the monocrystalline wafer not being adequate for this measurement system. Just one thicker (1µm) layer with dilution 2 gave as result a ratio of 0.076 which is considered to be a good value.

4.3 Cells

For the cell optimization the following procedure was applied. At first, a dilution series was carried out with fixed cell thickness of 180 nm at a set deposition temperature of 200°C. The dilution was chosen between ratio 1 and 64 in binary logarithmic steps. According to the results from the dilution series, the ideal gas flux was then set for a thickness series of cells with a protocrystalline i-layer. The selected i-layer thicknesses are all between 70 nm and 1 µm. After this second series, another series with deposition temperature variation was planned, but due to the temperature instabilities in the deposition chamber it was only partially done.

4.3.1 Influence of hydrogen dilution in the intrinsic layer

Figure 4.6 shows the results of the dilution series in chamber A. All the different substrates show a clear increase of the open-circuit voltage when the value of the gas flux dilution is increased, so when the material is going from the amorphous to the protocrystalline phase. When the material reaches the microcrystalline phase there is a steep decrease, due to the lower energy bandgap of microcrystalline material. On the left side, the measurements in the initial state are illustrated; on the right one, the measurements after light soaking. The cells of this series stayed at light soaking for more than 1000 hours (1127 to be precise), so the degraded state can be considered to be stabilized. A general decrease of the V_{oc} due to the light-induced degradation process is visible, for lower dilutions more remarkable as for higher one. Different reasons for that are currently being discussed in literature.

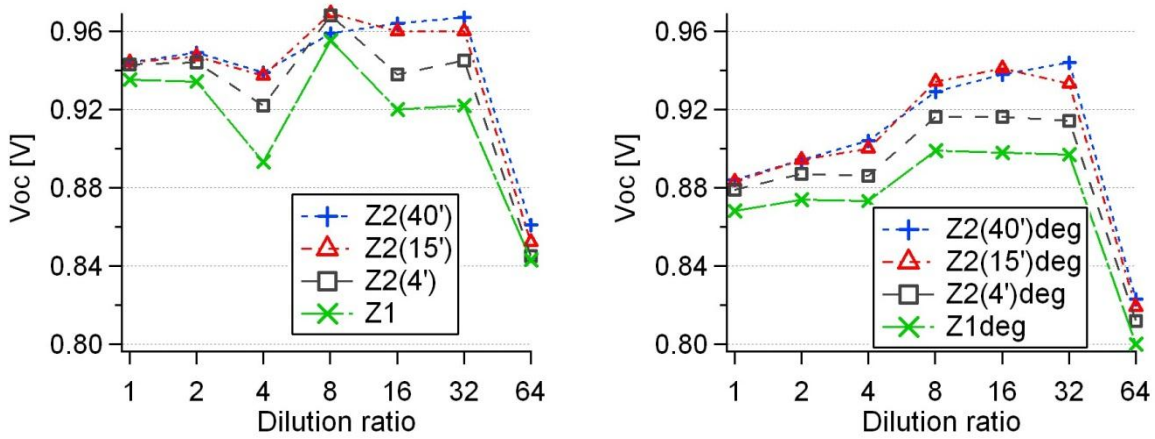

Figure 4.6: A slight increase of the Voc in the protocrystalline phase is remarkable in the initial state of the cell (left graph) and even better in the degraded state on the right.

Especially in the right graph the difference within the different substrates is visible. This is caused due to their different surface roughness. The TCO pyramids of the Z1 or Z2(4') substrates are higher and sharper, because they were not, or just shortly treated in contrast to the two other substrate types. Two different explanations can lead to the V_{oc} reduction seen. The first is that due to the bigger roughness the deposition surface is larger and so the layer thicknesses are smaller. Thinner doped layers can lead to a smaller built-in voltage and thus to a lower V_{oc}. The second possible explanation is that at the "valley points" between the pyramids, the formation of cracks, so micro-shunts, is more probable for rougher substrates. That would also reduce the V_{oc}. A combination of the two factors is possible too.

The point still having a good V_{oc} value and with the maximal dilution is the 32 dilution point, but first also the fill factor has to be analysed. In Figure 4.7 the FF values are represented, on the left in the initial state and on the right in the degraded state.

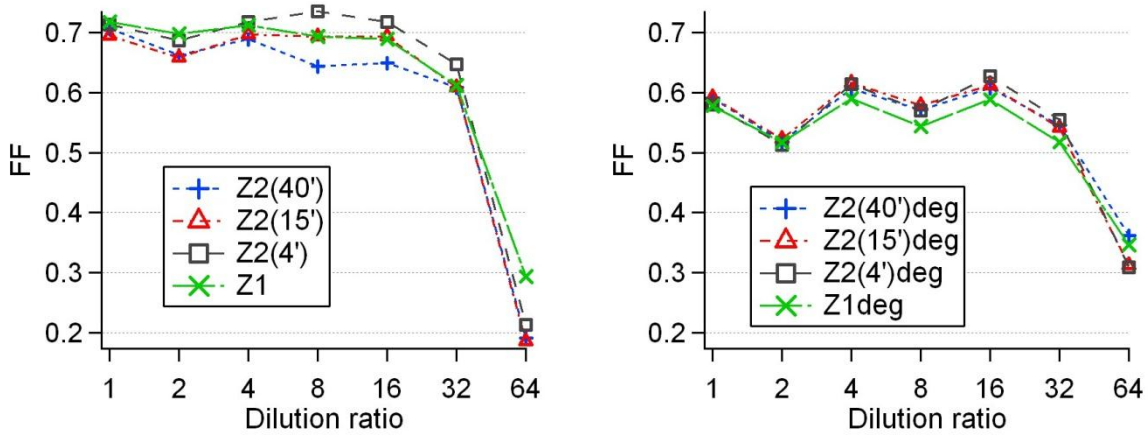

Figure 4.7: The FFs have an acceptable value till to the dilution of 16 or 32. Then its value decreases, because the IV curves start to show a s-shaped behaviour.

The FF graphs show a similar trend as the V_{oc} ones, in what concerns the decrease when the phase is entering the transition zone. However, the FF at dilution 32 is already lower than the precedent lower-dilution points. This could mean that with dilution 32 the crystalline zone is already reached and so rather dilution 16 should be chosen for the further thickness series.

To complete the analysis of the dilution series, the product of the V_{oc} and the FF is plotted in Figure 4.8. This is the most relevant factor for top cells.

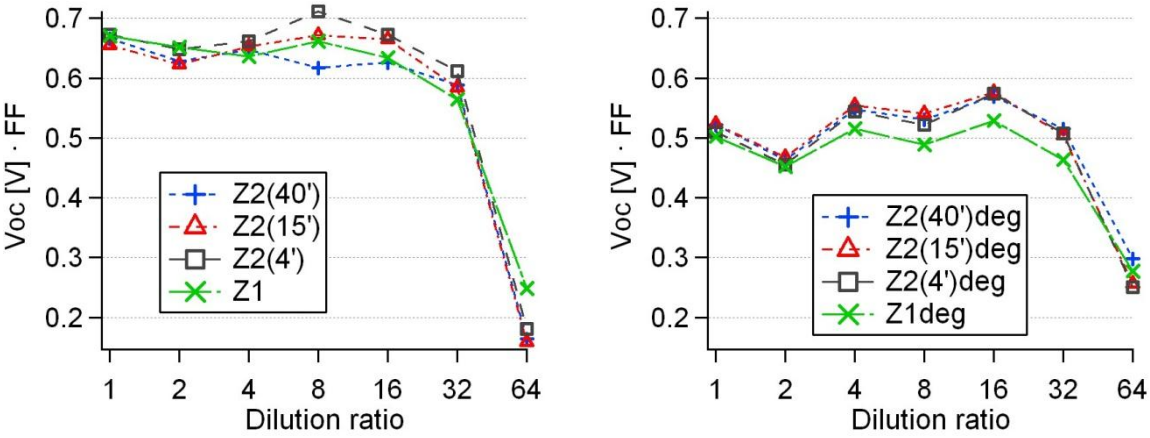

Figure 4.8: The product of the V_{oc} and the FF is the relevant value in this project and the two graphs clearly show its steep decrease when the intrinsic layers' material is entering the microcrystalline phase.

As observed before, the dilution 32 may already have passed the transition boundary to the microcrystalline part.

Figure 4.9 illustrates the IV curve development on dependence of the dilution. The curve of dilution 64 clearly shows that there is also a crystalline phase present in the layer, due to the s-shape behaviour. The 32 curve also already differs from the other ones. For this reason the thickness series has been carried out with the dilution 16. With this dilution the deposited intrinsic layer can, with high probability, be considered to be protocrystalline. However, to better understand this particular transition phase, also a thicker cell with the dilution 32 has been deposited.

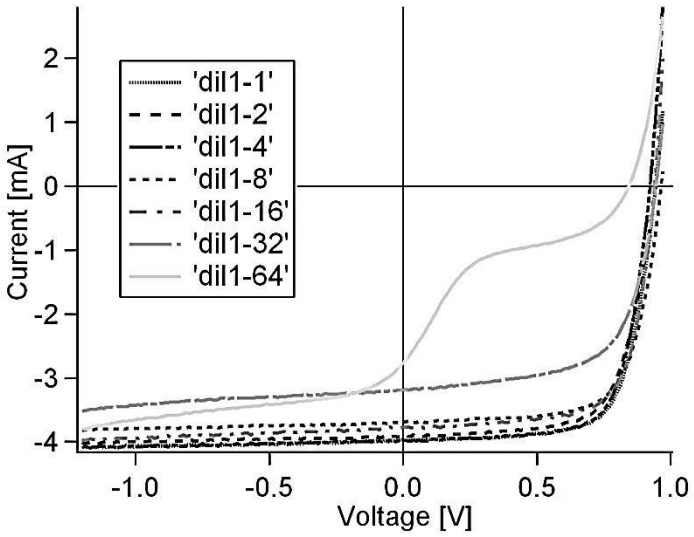

Figure 4.9: Comparison of the IV curves of the dilution series on the Z2(4') substrate. The cell with the 64 dilution ratio shows the particular s-shape behaviour.

The short-circuit current (J_{sc}) shows a decreasing trend with increasing dilution (see Figure 4.10). This can be explained thanks to the higher energy bandgaps at higher dilution illustrated in Figure 4.5. A higher energy band gap means a smaller part of the solar spectrum which can be absorbed, so a lower current. The cell with dilution 32, substrate Z2(40') in the initial state (left graph) was not considered, because the measured subcell was probably damaged.

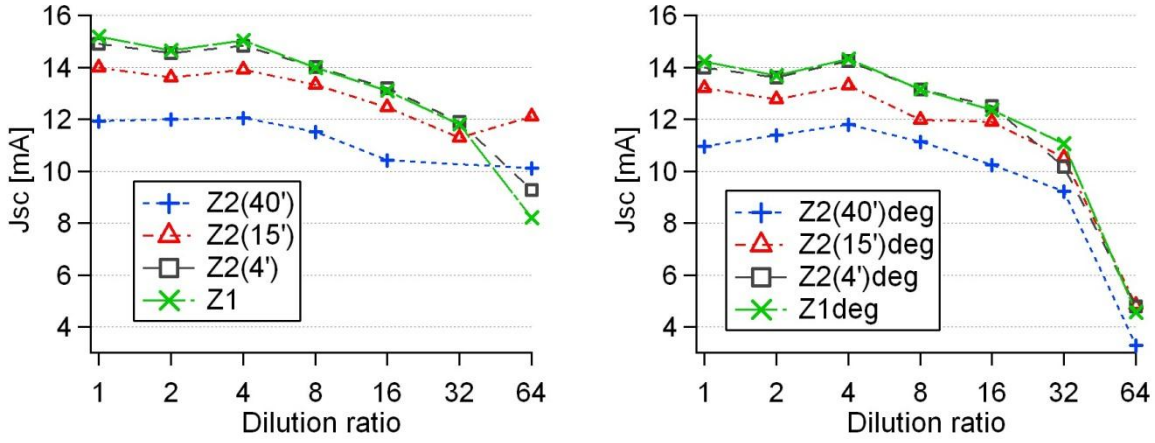

Figure 4.10: The short-circuit current is decreased for higher dilution ratios, due to the increase of the energy band gap.

This are the J_{sc} values measured with the EQE set-up. As example, the EQE curves of the four cells with dilution 2 (initial state) are represented in Figure 4.11. A clear difference between the four used substrates is visible. The higher light scattering in the cells with the Z1 and Z2(4') substrate leads to a higher absorption, so to a higher current [14].

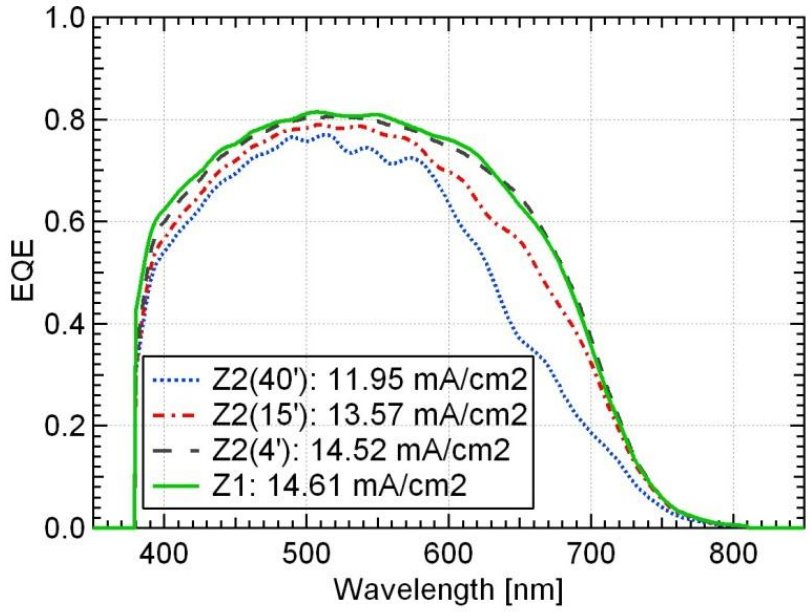

Figure 4.11: EQE of the dilution 2 cells in initial state. The differences in current between each substrate due to their different TCO/layer interface roughnesses are clearly visible.

4.3.2 Influence of intrinsic layer thickness

Due to the first results the gas flux dilution of 16 was taken as standard for this series. The variable parameter was now the thickness of the intrinsic layer. One point, with 180 nm thickness, was already given by the dilution series before. To extend the series, two thinner cells with 100 nm and 70 nm and three thicker cells with 300, 600 and 1000 nm thick i-layers were deposited. Depositions of such thick layers obviously needed some more time. The p-layers of the cells of this series were done in chamber D, due to technical problems in chamber C, but searching to keep exactly the same properties of the layer. The cell with the intrinsic layer of 600 nm on the Z2(40') substrate was excluded from the analysis, because it has probably been damaged during one of the processing steps and its results were thus not evaluable. The light soaking period for this series was not 1000 hours, but just around 550 hours due to the time limitation of this project. However, because of the exponentially decreasing effect of the light-induced degradation process, the first hundreds of hours are considered to be the essential ones.

As in the previous series, at first the V_{oc} results are presented in Figure 4.12, initial state on the left, degraded on the right. The thinner cells have a higher open-current voltage. At least in the initial state, shown in the left graph, this is well remarkable.

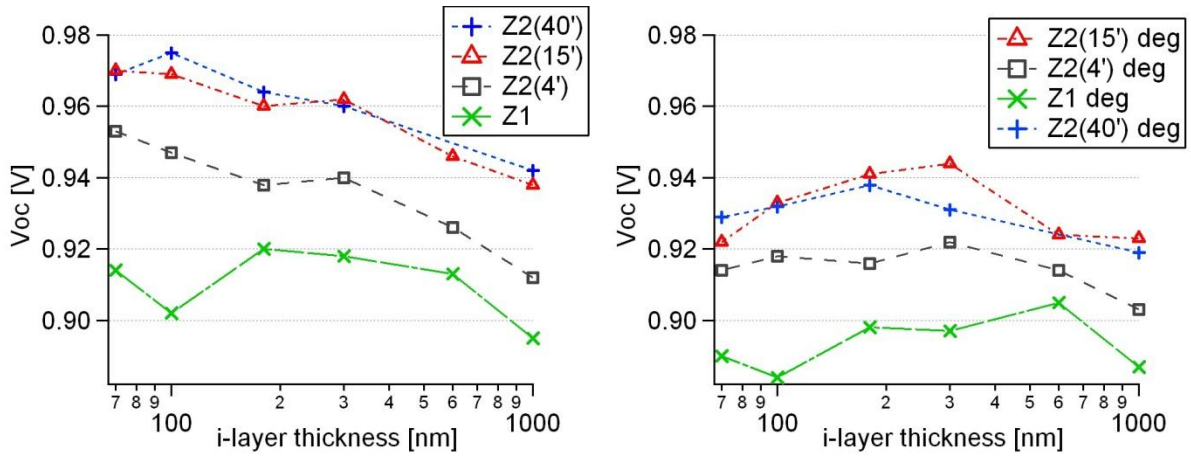

Figure 4.12: Semi-logarithmic diagram representing the V_{oc} dependence on the intrinsic layer thickness.

However, when the layer is getting too thin, cracks and so micro-shunts are more probable to be present and can lead to a V_{oc} reduction. In the initial state this just appears between 70 and 100 nm thickness. In the degraded state, however, the maximum V_{oc} is shifted to larger thickness.

Figure 4.13 illustrates the corresponding fill factors. Here, the trend of having better values for thin cells is evident, especially in the degraded state. This can well be explained using the formula of the recombination current density term introduced in section 2.1.1. This tells that the recombination current density J_{rec} not just increases proportionally to the photo generated current density J_{ph}, but has an ulterior factor which depends on the i-layer thickness (d) squared. J_{rec} has a direct consequence on the FF [7] and so the decrease in FF, when d is increased, makes sense. The light-induced degradation increases the J_{rec} by lowering the effective driftlength of the charged particles, so the factor with d squared additionally gains in importance and the FF decrease is even steeper for degraded cells.

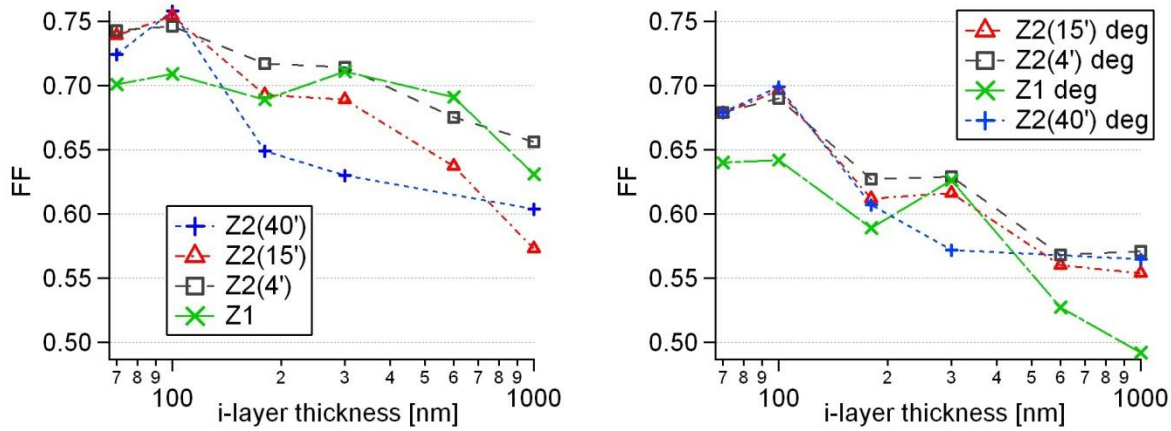

Figure 4.13: The fill factors of thinner cells are clearly better in the initial state and even more in the degraded state in comparison to the thicker ones.

Similar to the V_{oc} initial state diagram, the FF values of the 70 nm cells are already slightly reduced compared to the 100 nm ones. That could be explained again by microshunts for very thin cells.

Figure 4.14 finally shows the V_{oc} FF product. It is evident that the best cell was obtained with the 100 nm thick intrinsic layer. The difference comes mostly from the FF which shows a large dependence on the i-layer thickness.

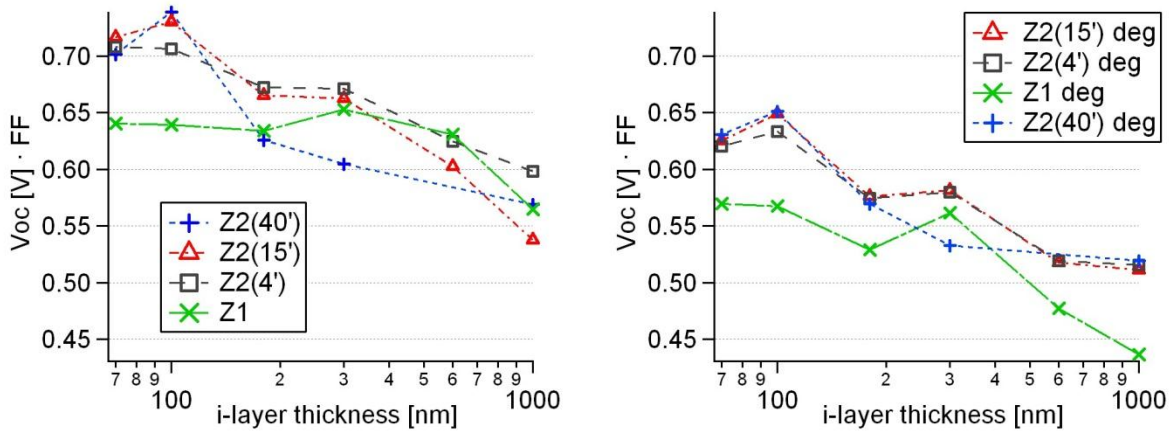

Figure 4.14: The fundamental factor V_{oc}·FF shows in both states that the thinner the cell, the better its value. However there is a limit in thinness due to probable micro-shunts and so a maximum at 100 nm.

When analysing the thickness series the current values were not completely neglected. Usually in triple cell the current is limited by the middle or bottom cell. However, if the current decreases too much, due to the thinness of the absorbing layer (see Figure 4.15) it could fall beyond the minimal current limit given by the other cells. This has to be avoided.

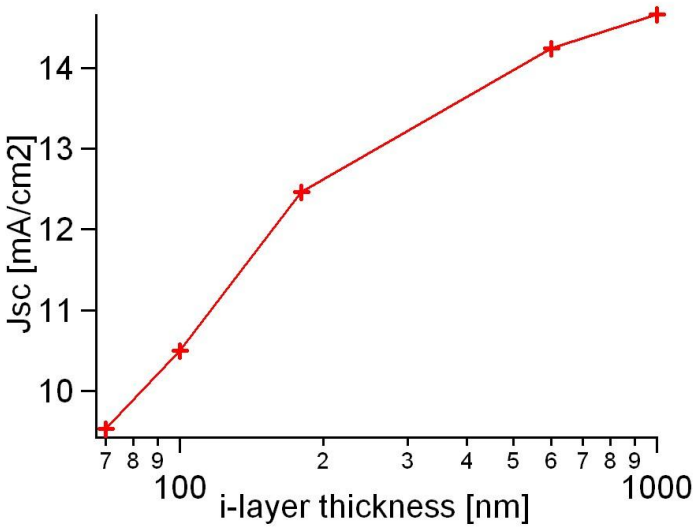

Figure 4.15: Current decrease (in initial state and with the Z2(15') substrate) due to the thinner i-layer in which the photons are absorbed.

The current density shows this trend for all substrates and in both states. In the degraded state the values are additionally decreased by 5 to 10 %, for thicker cells even more.

In Table 4.1, the relevant parameters of the best two subcells (cells with 100 nm thick i-layer on the substrate Z2 15' and Z2 40') are resumed. The Voc and FF product is very promising, but the current is too low for the use in triple cells. In particular, it has to be noticed that the EQE measurements were carried out with a white blackreflector, what does not correspond to the reality of a top cell where the current would be even lower.

Dilution ratio	d_i [nm]	Substrate	State	Subcell no.	Voc [V]	FF	Voc[V]·FF	J [mA/cm2]	Eff [%]
16	100	Z2(40')	ini	1	0.975	0.758	0.739	9.43	6.969
16	100	Z2(40')	deg	1	0.932	0.699	0.652	8.74	5.694
16	100	Z2(15')	ini	13	0.969	0.754	0.731	10.5	7.672
16	100	Z2(15')	deg	13	0.933	0.696	0.649	9.79	6.357

Table 4.1: The most important values of the two best cells resumed. Good Voc·FF product, but quite low current values.

The Raman crystalliniy of some cells was measured, but even the 1µm thick cell with dilution ratio 16 did not show crystallinity, what means that they were all still in the protocrystalline phase. The layer with 16 dilution ratio on glass already showed a small crystalline peak at a thickness of around 110nm. However, it is known that the substrate has an influence on the transition boundary [11].

To analyse a cell that has an intrinsic layer which passes from protocrystalline to microcrystalline silicon, a cell was deposited with a dilution ratio of 32 and a thickness of 1µm. De facto, this cell had a crystallinity factor of around 75 % on the n-side, while the material at the p- or glass side was still amorphous (see Figure 4.16).

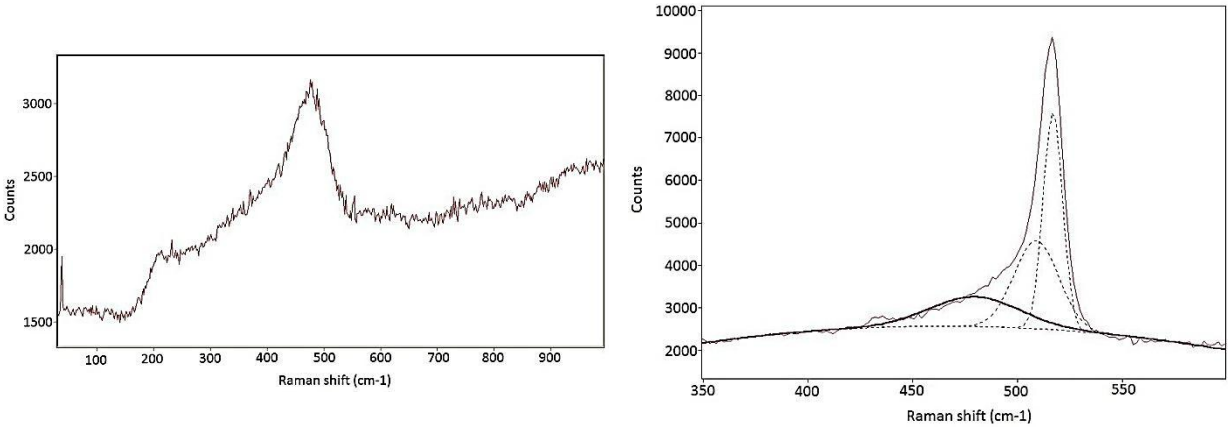

Figure 4.16: Raman measurements on the p-side (left) and on the n-side (right) of the 1µm thick cell with dilution 32. On the n-side the microcrystalline material is dominant.

In the left image (p-side) the Raman curves does not show any peak above 500 cm-1, so the material is still completely amorphous. On the n-side, in contrast, the crystalline peak is clearly visible.

The EQE and IV curves also show a very particular behaviour of this cell (see Figure 4.17).

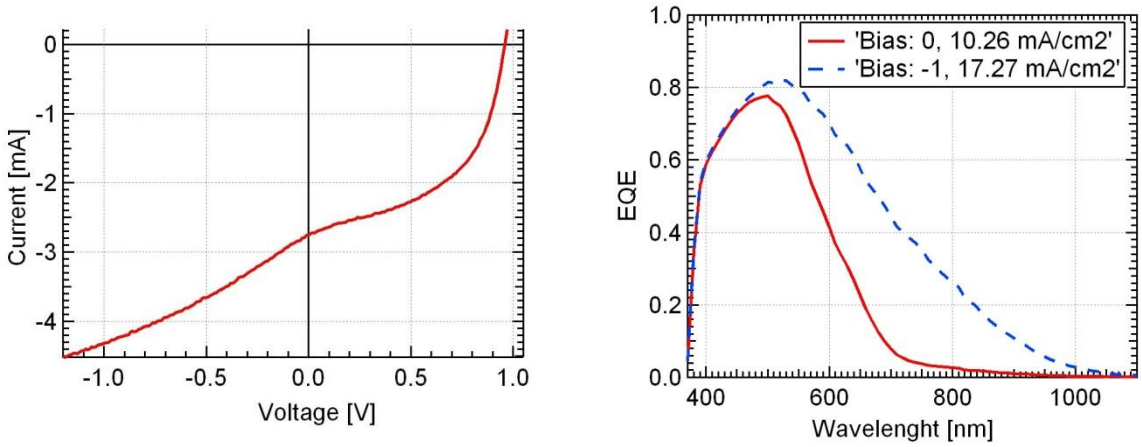

Figure 4.17: IV and EQE curves of the subcell number 13 with dilution ratio 32 and 1µm thickness on Z2(15'). They confirm the presence of both, amorphous and microcrystalline material in the intrinsic layer.

This cell has some combined characteristics of both, amorphous and microcrystalline material. The V_{oc} is high (0.959 V) and due to the transition to microcrystalline material a high current is measured when applying the reverse bias too. This transition also causes the s-shaped IV curve. Usually for amorphous cells the EQE measurement is carried out in the range between 370 nm and 810 nm. For this cell the range had to be extended to the range of microcrystalline cells (till 1100 nm). The EQE curve with the reversed bias going beyond the 800 nm, shows that photons with lower energy are absorbed (because of the presence of microcrystalline material that has a lower bandgap), but for no bias applied they are not collected. There is probably an additional potential step due to the phase transition in the i-layer, which limits the charge collection.

The FF of 0.505 is obviously not good for a cell, but these insights of cell's properties could be relevant for further researches.

To check, if the assumption about the transition from amorphous to microcrystalline silicon in the intrinsic layer was correct (but also for further analysis), the cell deposited on a Z2(15') substrate with dilution 32 and with the 1 µm thick i-layer was imaged by TEM (see Figure 4.18).

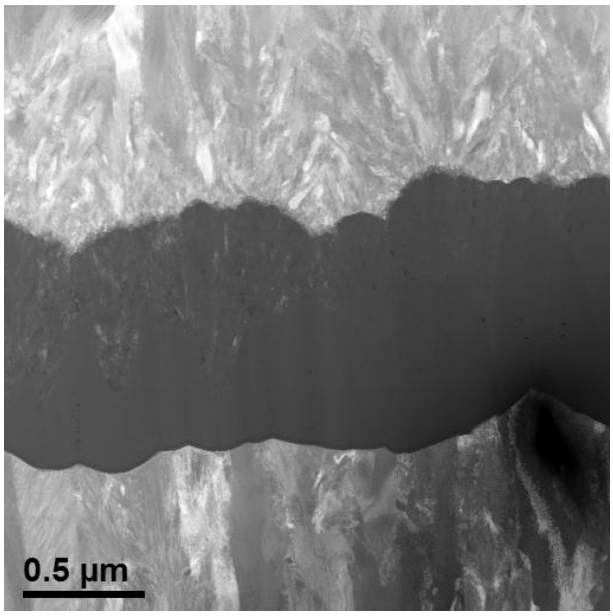

Figure 4.18: TEM image of the 1 µm thick cell: the silicon layer (dark) is sandwiched by the ZnO front and back contact. It is clearly visible that at a certain thickness, crystallites start to evolve and the silicon material becomes microcrystalline. Image done by D. Alexander.

The image confirmed the assumption by showing the transition from amorphous to microcystalline silicon within the layer. Beside of that another particular structure is apparent: starting from the front contact peaks, vertical sequences of tiny impurities seem to be present. However, it has to be clarified first if they are not artefact effects.

4.3.3 Influence of deposition temperature

Instead of a series, just some tests were carried out for the deposition temperature analysis because of the already mentioned instabilities. Hence tests with large deposition temperature differences were done, in order to see a possible trend. Four cells with the dilution ratio of 16 were deposited in total. Their deposition temperatures for each layer and their i-layer thicknesses are resumed in Table 4.2. As in the thickness series the p-layers of these cells were deposited in chamber D.

Cell's name	d_i [nm]	T for p-layer	T for i-layer	T for n-layer
Ti160	180	200	160	200
Tp160	180	160	200	200
Tp+i160	180	160	160	200
Ti160th100	100	200	160	200

Table 4.2: Summary of the deposition temperature tests carried out. The dilution ratio was of 16.

Figure 4.19 shows the measured V_{oc}. In order to do a comparison with the values obtained before, the data of the two corresponding cells (with 100 nm and 180 nm i-layer thickness) are added to the graph. They are called Standard180 and Standard100 referring to their standard deposition temperature and their thickness. The light soaking period was around 570 hours.

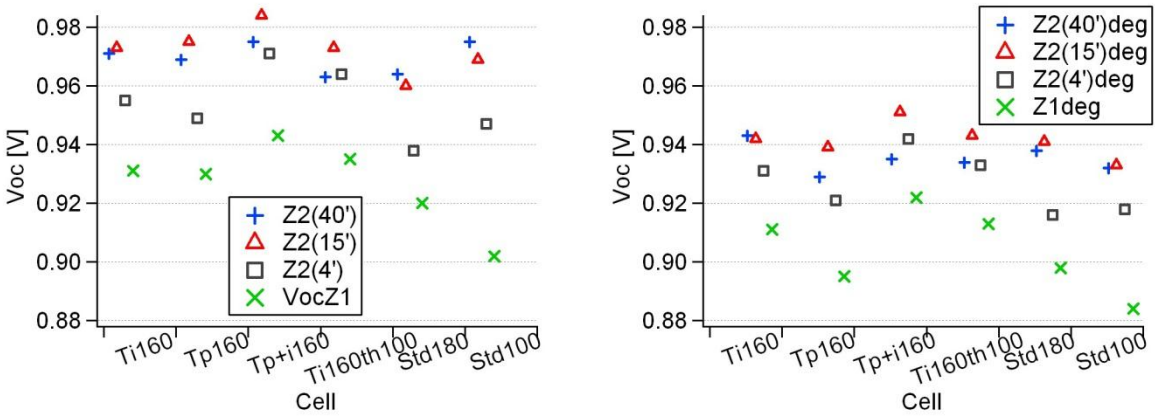

Figure 4.19: V_{oc} comparison of the cells with lower deposition temperatures with the standard cells obtained during the series before, on the left the initial values, on the right the degraded ones.

The expectation of having a slight increased V_{oc} for lower deposition temperature is confirmed in the most cases, in the initial as well as in the degraded state. Figure 4.20 illustrates the corresponding FF values.

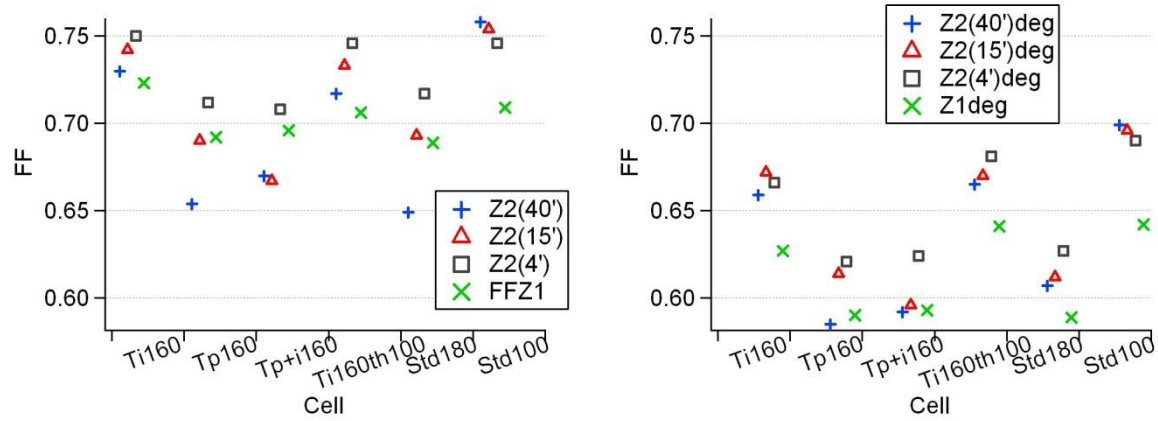

Figure 4.20: The fill factors in the initial (left) and degraded (right) state have in general a similar value to their corresponding cell, deposited at standard deposition temperature. Just Ti160 has a noticeable better value than its corresponding standard cell.

The Ti160 cell has better FF values in comparison to its corresponding standard cell, while the other cells do not show considerably differences in comparison to the other cells having the same i-layer thickness. The good V_{oc} and FF values lead to similarly good products. These are plotted in Figure 4.21.

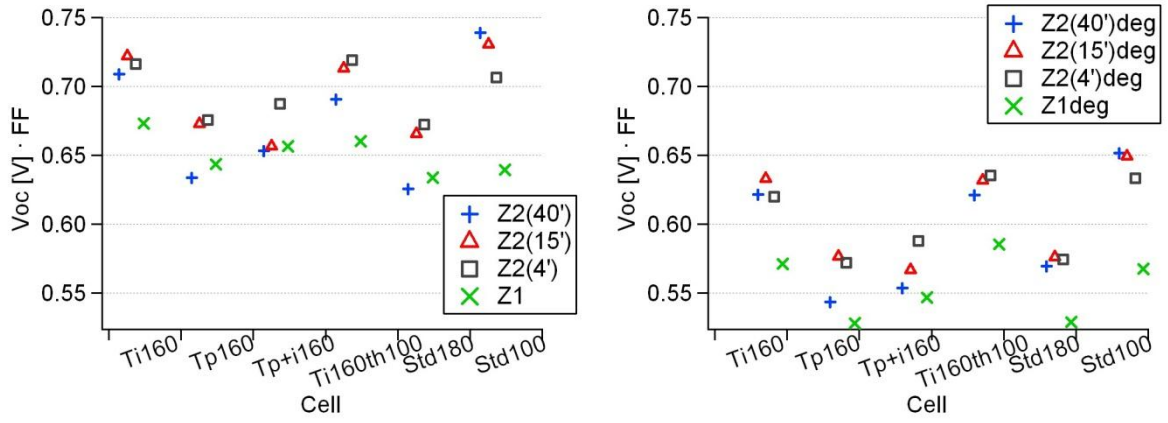

Figure 4.21: Considering the Voc and FF product the cell with the 100 nm thick i-layer and the standard deposition temperatures still has the highest values in the initial state (left) and the degraded state (right).

The Standard 100 cell obtained in the previous series still has the best V_{oc}·FF products; however the Ti160 has the advantage, due to its thicker i-layer to have a larger current. The current densities measured for these cells are mostly equivalent to the ones measured in the thickness series, so the principal factors influencing the current are the intrinsic layer thickness and the substrate roughness.

4.4 Triple-junction cell

During the last days of the project it was tried to include the top cell in a triple cell deposition. Due to modifications carried out at the deposition system during the revision and the fact of having just one try reduced by far the chance of depositing a good cell.

As top cell, the recipe with dilution 16 and the intrinsic layer with a thickness of 180 nm deposited at 160°C was chosen. For the deposition 4 different substrates were used. Two B52 front contacts treated with argon for 7 minutes, a double layer front contact (20 min treatment) and a Z1 (15 min treatment). After the top cell deposition, one B52(7) substrate was back contacted in order to measure its cell properties as single junction. On the remaining three top cells, the middle and the bottom cell were deposited in another deposition system, called system B.

For the top cell a V_{oc} of 0.964 V and a FF of 73.7 % were obtained, which results in a product of 0.71 V. These good values reproduce what was obtained in the previous section for the equivalent Ti160 cell.

For the best triple-junction cell, which was the one on the double layer front contact treated for 20 min, a V_{oc} of 1.883 V and a FF of 75.4 % were obtained. The measurements with the EQE set-up gave current densities of 8.59 mA/cm^2 for the top cell, 7.89 mA/cm^2 for the middle cell and 8.73 mA/cm^2 for the bottom cell. The middle cell limits the total current density and this current mismatch also causes an overestimation of the FF during the IV measurement. For this reason the calculated efficiency of 11.2 % is also an overestimation.

For the optimization of a triple-junction cell more time should be necessary. Hence this last part is considered an interesting final experiment, but not relevant for concrete conclusions.

5. Conclusions and outlook

Starting from the dilution series it was possible to find the hydrogen/silane flux ratio for obtaining protocrystalline silicon. It has been shown that using a dilution factor between 16 and 32 this transition phase between amorphous and microcrystalline silicon can be deposited. Protocrystalline silicon has a higher energy bandgap and this was also confirmed in the cell dilution series when higher V_{oc} were obtained for the dilutions 16 and 32. However, it seems that the FF decreases before the V_{oc} when the material is becoming crystalline. For this reason the second series in which the thicknesses of the intrinsic layers were varied, was carried out with a dilution of 16.

The thickness series showed clear better cells for thin intrinsic layers in term of V_{oc} and FF product. The best V_{oc} and FF values were 0.975 V and 75.8% (0.932 V and 69.9 %) in initial (degraded) state. These were obtained with the cell deposited on a Z2(15') substrate and with the 100 nm thick intrinsic layer. Nevertheless, due to the thin absorbing layer, the current density is considerably decreased. Thus the use in practical application strongly limited.

However, in the last part it was demonstrated, that similar high V_{oc} and FF values can be obtained for a thicker cell (with a 180 nm i-layer) by decreasing the deposition temperature. Such a cell would be rather considered in the application as top cell in a triple junction cell.

In addition by depositing in the transition regimes between microcrystalline and amorphous silicon, particular cells could be analyzed. Some still having a high V_{oc} (when approaching the transition from the amorphous part) but already absorbing photons in the spectral range where usually just microcrystalline cells do absorb. These are interesting insights which stimulate to further investigations.

6. Comments and acknowledgements

At the end of my studies in physics it was very satisfying to me to have the opportunity to apply the knowledge acquired during the study on a subject field of practical use and public interest. Surely the results of this thesis will not be the proof for any revolutionary statements, but at least they may contribute to advance a bit in this research field.

Special thanks go to Michael STUCKELBERGER who introduced me to the laboratory and for his advices during the entire project. I am also grateful to Dr. Matthieu DESPEISSE and Prof. Cristophe BALLIF which gave me the possibility to join the PV-Lab group during this project and to Duncan ALEXANDER who did the nice TEM image at the EPFL.

All the staff within the research group was always cooperative and helpful what simplified by far my stay in Neuchâtel. Thanks you!

Fabio MAURIZIO

Abbreviations and symbols

AM1.5G	Air mass coefficient with 1.5 atmosphere thickness and global irradiance
AM0	Air mass coefficient outside atmosphere
c	Speed of light
EQE	External quantum efficiency
CIGS	Copper-indium-gallium-selenide
CVD	Chemical vapour deposition
d	Thickness of the i-layer
DEZ	Diethyl-zinc
E	Energy
E_g	Energy bandgap
E_{ph}	Energy of the photon
FF	Fill factor
FTIR	Fourier transform infrared spectroscopy
h	Planck constant
IPL	Ion projection lithography
I	Current
J_{ph}	Photo generated current density
J_{rec}	Recombination current density
J_{sc}	Short circuit current density
LP-CVD	Low pressure chemical vapour deposition
MPP	Maximum power point
OES	Optical emission spectroscopy
PECVD	Plasma enhanced chemical vapour deposition
PTFE	Polytetrafluoroethylene
PV	Photovoltaic
q (or e)	Elementary charge
R	Microstructure factor
R_s	Series resistance
R_{sc}	Short circuit resistance
sccm	Standard cubic centimeters per minute
SEM	Scanning electron microscope
Si:H	Hydrogenated silicon
SR	Spectral response
STC	AM1.5G normalized to 1000 W/m^2 and 25°C
T	Temperature
TCO	Transparent conducting oxide
TMB	Trimethylborane
V	Voltage
V_{bi}	Bias voltage
V_{oc}	Open circuit voltage
λ	Wavelength
μ	Mobility
τ	Life or capture time
ν	Wave frequency
$\Phi_{AM1.5}$	Solar spectrum at AM1.5G
Φ_{crist}	Raman crystallinity factor

Bibliography

[1] S. Nowak, “Photovoltaik Potenziale Schweiz / EU,” Bundesamt für Energie BFE, Bern, 2010.

[2] T. Hostettler, “Markterhebung Sonnenenergie 2010 (Teilstatistik der Schweizerischen Statistik der erneuerbaren Energien),” Bundesamt für Energie BFE und Swissolar, Bern, 2011.

[3] Inventux, “ Solar Technolgies,” [Online]. Available: http://inventux.de/produkte/solar-modules. [Accessed 7 1 2012].

[4] Y. Baojie et al., “Effect of hydrogen dilution on the open-cirucit voltage of hydrogenated amorphous silicon solar cells,” Appl. Phys. Lett. 83 (4), 2003.

[5] A. V. Shah (Ed.), Thin-Film Silicon Solar Cells, Lausanne: EPFL Press, 2010.

[6] L. Kazmerski, *NREL compilation of best research solar cell efficiencies,* US Department of Energy: National Renewable Energy Laboratory (NREL), March 2011.

[7] J. Merten et al., “Improved Equivalent Circuit and Analytical Model for Amorphous Silicon Solar Cells and Modules,” IEEE TRANSACTIONS ON ELECTRON DEVICES, VOL. 45, NO. 2, 1998.

[8] A. De Vos, “Detailed balance limit of the efficiency of tandem solar cells,” J. Phys. D: Appl. Phys., 13, Printed in Great Britain, 1980.

[9] J. Koh et al., “Optimization of hydrogenated amorphous silicon p–i–n solar cells with two-step i layers guided by real-time spectroscopic ellipsometry,” Appl Phys Lett 73, 1526, American Institute of Physics, 1998.

[10] R. Collins et al., “Advances in plasma-enhanced chemical vapor deposition of silicon films at low temperatures,” Elsevier, The Pennsylvania State University, 2002.

[11] J. Bailat et al., “Influence of substrate on the microstructure of microcrystalline silicon layers and cells,” ELSEVIER, Neuchâtel, 2002.

[12] D. L. Staebler et al., “Reversible conductivity changes in discharge-produced amorphouos Si,” Applied Physics Letters 31 (4), Princeton, New Jersey, 1977.

[13] J. Bailat et al., “High-efficiency pin microcrystalline and micromorph thin film silicon solar cells deposited on LPCVD ZnO coated glass substrates,” WCPEC, Waikoloa, HI, 2006.

[14] J. Müller et al., “TCO and light trapping in silicon thin film solar cells,” ELSEVIER, Jülich, Germany, 2004.

[15] D. M. Mattox, Handbook of Physical Vapor Deposition (PVD) Processing, Oxford UK: Elsevier, 2010.

[16] R. Platz, “Amorphous silicon for optimized multi-junction solar cells: Material study and cell design,” PhD thesis, University of Neuchâtel, 1999.

[17] U. Kroll et al., “Potential of VHF-plasmas for low-cost production of a-Si:H solar cells,” ELSEVIER, Neuchâtel, 1997.

[18] M. Zeman et al., “Optical and electrical modeling of thin-film silicon solar cells,” Material Research Society, Vol. 23 No. 4, Delft University, The Netherlands, 2008.

List of figures

List of tables

Appendixes

Table with the Voc, FF and Voc·FF values used for the dilution and thickness series plots:

Dilution Series	Z2(40)				Z2(15)				Z2(4)				Z1			
	Voc[mV]	FF	VocFF	cell	Voc[mV]	FF	VocFF	cell	Voc[mV]	FF	VocFF	cell	Voc[mV]	FF	VocFF	cell
Oa111109dil1-1	0.944	0.706	0.6665	2	0.944	0.694	0.6551	8	0.943	0.713	0.6724	8	0.935	0.717	0.6704	5
Oa111102dil1-2	0.949	0.662	0.6282	1	0.947	0.658	0.6231	8	0.944	0.687	0.6485	6	0.934	0.698	0.6519	7
Oa111101dil1-4	0.939	0.689	0.647	1	0.937	0.697	0.6531	6	0.922	0.717	0.6611	1	0.893	0.712	0.6358	5
Oa111109dil1-8	0.959	0.644	0.6176	9*	0.969	0.693	0.6715	11*	0.968	0.735	0.7115	2*	0.955	0.693	0.6618	1
Oa111101dil1-16	0.964	0.649	0.6256	3*	0.96	0.693	0.6653	4	0.938	0.717	0.6725	6	0.92	0.689	0.6339	5
Oa111102dil1-32	0.967	0.609	0.5889	9*	0.96	0.608	0.5837	15	0.945	0.647	0.6114	5	0.922	0.612	0.5643	4
Oa111101dil1-64	0.861	0.191	0.1645	4	0.852	0.186	0.1585	13	0.845	0.214	0.1808	13	0.843	0.294	0.2478	4
* values calculated with IgorSoftware for this subcell																
after degradation																
Oa111109dil1-1	0.884	0.591	0.5224	16	0.883	0.592	0.5227	15	0.879	0.58	0.5098	8	0.868	0.578	0.5017	13
Oa111102dil1-2	0.894	0.518	0.4631	1	0.894	0.523	0.4676	8	0.887	0.513	0.455	6	0.874	0.517	0.4519	7
Oa111101dil1-4	0.904	0.606	0.5478	1	0.9	0.616	0.5544	15	0.886	0.614	0.544	7	0.873	0.59	0.5151	1
Oa111109dil1-8	0.929	0.571	0.5305	10	0.934	0.579	0.5408	14	0.916	0.57	0.5221	13	0.899	0.544	0.4891	7
Oa111101dil1-16	0.938	0.607	0.5694	5	0.941	0.612	0.5759	1	0.916	0.627	0.5743	6	0.898	0.589	0.5289	5
Oa111102dil1-32	0.944	0.546	0.5154	15	0.933	0.541	0.5048	1	0.914	0.555	0.5073	4	0.897	0.517	0.4637	4
Oa111101dil1-64	0.823	0.362	0.2979	8	0.819	0.312	0.2555	16	0.812	0.309	0.2509	1	0.8	0.347	0.2776	16
Thickness Series																
Oa111125dil1-16(1µm)	0.942	0.604	0.569	16	0.938	0.573	0.5375	1	0.912	0.656	0.5983	13	0.895	0.631	0.5647	8
Oa111128th600	0.667	0.352	0.2348	10	0.946	0.637	0.6026	13	0.926	0.675	0.6251	5	0.913	0.691	0.6309	5
Oa111129th300	0.96	0.63	0.6048	13	0.962	0.689	0.6628	15	0.94	0.714	0.6712	5	0.918	0.711	0.6527	5
Oa111101dil1-16(180nm)	0.964	0.649	0.6256	3*	0.96	0.693	0.6653	4	0.938	0.717	0.6725	6	0.92	0.689	0.6339	5
Oa111128th100	0.975	0.758	0.7391	1	0.969	0.754	0.7306	13	0.947	0.746	0.7065	13	0.902	0.709	0.6395	13
Oa111201th70b	0.969	0.724	0.7016	3	0.97	0.739	0.7168	3	0.953	0.743	0.7081	13	0.914	0.701	0.6407	5
after degradation																
Oa111125dil1-16(1µm)	0.919	0.565	0.5192	16	0.923	0.554	0.5113	1	0.903	0.571	0.5156	13	0.887	0.492	0.4364	4
Oa111128th600					0.924	0.56	0.5174	16	0.914	0.568	0.5192	5	0.905	0.527	0.4769	1
Oa111129th300	0.931	0.572	0.5325	13	0.944	0.616	0.5815	5	0.922	0.629	0.5799	8	0.897	0.626	0.5615	12
Oa111101dil1-16(180nm)	0.938	0.607	0.5694	5	0.941	0.612	0.5759	1	0.916	0.627	0.5743	6	0.898	0.589	0.5289	5
Oa111128th100	0.932	0.699	0.6515	1	0.933	0.696	0.6494	13	0.918	0.69	0.6334	5	0.884	0.642	0.5675	13
Oa111201th70b	0.929	0.679	0.6308	1	0.922	0.678	0.6251	16	0.914	0.679	0.6206	13	0.89	0.64	0.5696	1

Table with the Voc, FF and Voc·FF values used for the temperature series plots:

Temperature variation	Z2(40)				Z2(15)				Z2(4)				Z1			
	Voc[mV]	FF	VocFF	cell	Voc[mV]	FF	VocFF	cell	Voc[mV]	FF	VocFF	cell	Voc[mV]	FF	VocFF	cell
Oa111129Ti160	0.971	0.73	0.7088	5	0.973	0.742	0.722	1	0.955	0.75	0.7163	6	0.931	0.723	0.6731	5
Oa111129Tp160	0.969	0.654	0.6337	5	0.975	0.69	0.6728	9	0.949	0.712	0.6757	13	0.93	0.692	0.6436	1
Oa111202Tp+i160	0.975	0.67	0.6533	13	0.984	0.667	0.6563	3	0.971	0.708	0.6875	2	0.943	0.696	0.6563	8
Oa111202Ti160th100	0.963	0.717	0.6905	14	0.973	0.733	0.7132	5	0.964	0.746	0.7191	5	0.935	0.706	0.6601	5
after degradation																
Oa111129Ti160	0.943	0.659	0.6214	14	0.942	0.672	0.633	13	0.931	0.666	0.62	5	0.911	0.627	0.5712	8
Oa111129Tp160	0.929	0.585	0.5435	5	0.939	0.614	0.5765	13	0.921	0.621	0.5719	8	0.895	0.59	0.5281	16
Oa111202Tp+i160	0.935	0.592	0.5535	13	0.951	0.596	0.5668	4	0.942	0.624	0.5878	8	0.922	0.593	0.5467	8
Oa111202Ti160th100	0.934	0.665	0.6211	13	0.943	0.67	0.6318	5	0.933	0.681	0.6354	8	0.913	0.641	0.5852	5

Table with the deposition times and layer thicknesses used for the deposition rate plot:

ChA									**ChB**						
	Deposition time	**Thickness [nm]**					**deposition rate**			**Deposition time**	**Thickness [nm]**				**deposition rate**
Dilution	**[min]**	**1st**	**2nd**	**3rd**	**4th**	**average**	**[Å/s]**		**Dilution**	**[min]**	**1st**	**2nd**	**3rd**	**average**	**[Å/s]**
1:1	15	189	191	192		191	2.12		1:1	21	2010	2012	2025	2016	16.00
1:2	20	219	221	224	222	222	1.85		1:2	20	1371	1389	1381	1380	11.50
1:4	20	182	185	186		184	1.54		1:4	20	794	777	768	780	6.50
1:8	20	148	147	148		148	1.23		1:8	20	109	104	107	107	0.89
1:16	20	112	110	112	110	111	0.93		1:16	20	234	240	228	234	1.95
1:32	40	125	123	127		125	0.52		1:32	20	174	172	174	173	1.44
1:48	70	188	193	187		189	0.45		1:64	20	26	46		36	0.30
1:64	40	85	86	86	90	87	0.36		**Control or repetition tests:**						
									1:16b	20	236	233	235	235	1.96
									1:8b	20	320	328	324	324	2.70
									1:64b	40	199	199	200	199	0.83

Summary of all results in chronological sequence:

Cell ID	Substrat	Cell no.	Voc [V]	Isc [mA/cm2]	FF	VocFF	Rsc [Ω cm2]		Isc (EQE)	Eff [%]
Oa110928a	Z1	3	0.814	17.286	0.59	0.480	1596.292		16.15	7.76
	Z1	9	0.813	17.283	0.612	0.498	1738.887		16.15	8.04
	Z1	3	0.82	15.171	0.613	0.503	2252.753		16.03	8.06
	Z1	7	0.825	19.602	0.616	0.508	1352.177		16.22	8.24
degraded	Z1	3	0.859	16.158	0.486	0.417	618.021		14.92	6.23
	Z1	9	0.857	16.096	0.505	0.433	677.857		15	6.49
	Z1	3	0.859	14.133	0.497	0.427	795.606		14.91	6.37
	Z1	7	0.856	18.542	0.51	0.437	645.008		14.99	6.54
Oa110928b	Z1	7	0.883	14.004	0.752	0.664	2537.77		15.42	10.24
	Z1	7	0.883	17.338	0.749	0.661	1940.114		15.69	10.38
	Z1	7	0.884	17.505	0.753	0.666	1554.952		15.65	10.42
	Z1	7	0.89	14.57	0.752	0.669	1768.391		15.43	10.33
degraded	Z1	14	0.844	11.7	0.648	0.547	1283.214		14.5	7.93
	Z1	7	0.857	14.311	0.629	0.539	939.464		14.37	7.75
	Z1	7	0.851	16.517	0.637	0.542	926.782		14.56	7.89
	Z1	6	0.845	14.014	0.649	0.548	917.61		13.4	7.35
Oa110930a	Z1	7	0.905	14.699	0.752	0.681	2036.197		15.37	10.46
	Z1	6	0.906	14.7	0.749	0.679	3212.67		15.38	10.44
	Z1	14	0.902	14.606	0.755	0.681	2351.949		15.36	10.46
	Z1	6	0.904	14.595	0.748	0.676	2866.844		15.33	10.37
degraded	Z1	7	0.864	13.836	0.648	0.560	1075.659		14.54	8.14
	Z1	6	0.861	12.957	0.648	0.558	1139.579		14.56	8.12
	Z1	14	0.867	12.77	0.654	0.567	1133.553		14.6	8.28
	Z1	6	0.866	12.999	0.641	0.555	1156.233		14.56	8.08
Oa111003a	Z1	8	0.923	15.083	0.704	0.650	4070.37		15.67	10.18
	Z1	15	0.922	15.069	0.711	0.656	2925.176		15.67	10.27
	Z1	6	0.928	15.125	0.705	0.654	3211.277		15.75	10.30
	Z1	5	0.926	15.054	0.704	0.652	2229.093		15.75	10.27
degraded	Z1	8	0.864	14.285	0.54	0.467	724.911		14.69	6.85
	Z1	15	0.858	12.528	0.555	0.476	949.117		14.63	6.97
	Z1	6	0.866	13.167	0.534	0.462	746.845		14.66	6.78
	Z1	5	0.869	14.189	0.538	0.468	766.847		14.67	6.86
Oa111019dil1-1	Z2(40)	12	0.945	10.633	0.66	0.624	1501.244		11.69	7.29
	Z2(15)	13	0.931	11.797	0.606	0.564	772.45		12.65	7.14
	Z2(4)	1	0.939	12.71	0.651	0.611	1213.432		13.35	8.16
	Z1	10	0.877	12.909	0.594	0.521	1117.704		13.44	7.00
degraded	Z2(40)	12	0.88	9.128	0.463	0.407	436.243		9.53	3.88
	Z2(15)	13	0.862	10.139	0.451	0.389	379.369		10.55	4.10
	Z2(4)	1	0.879	11.145	0.478	0.420	470.254		11.56	4.86
	Z1	10	0.858	11.277	0.457	0.392	391.422		11.53	4.52
Oa111019dil1-4	Z2(40)	3	0.948	10.423	0.601	0.570	1433.113		11.45	6.52
	Z2(15)	9	0.746	11.879	0.37	0.276	179.337		12.16	3.36
	Z2(4)	15	0.95	12.647	0.631	0.599	1187.583		13.48	8.08
	Z1	5	0.904	13.048	0.539	0.487	938.557		13.58	6.62
degraded	Z2(40)	3	0.876	9.823	0.462	0.405	618.977		10.65	4.31
	Z2(15)	9	0.648	11.257	0.376	0.244	154.957			
	Z2(4)	15	0.889	9.901	0.503	0.447	932.091		12.74	5.70
	Z1	5	0.85	12.12	0.444	0.377	457.028		12.67	4.78
Oa111019dil1-16	Z2(40)	15	0.88	10.411	0.439	0.386	275.165		10.06	3.89
	Z2(15)	15	0.548	11.541	0.316	0.173	80.203		10.86	1.88
	Z2(4)	11	0.903	11.931	0.486	0.439	409.659		12.28	5.39
	Z1	15	0.74	11.786	0.422	0.312	247.614		11.86	3.70
degraded	Z2(40)	15	0.765	7.155	0.381	0.291	270.599		9.74	2.84
	Z2(15)	15	0.462	11.152	0.312	0.144	62.714		9.26	1.33
	Z2(4)	6	0.861	11.228	0.481	0.414	439.287		11.41	4.73
	Z1	15	0.712	10.972	0.402	0.286	216.734		10.57	3.03

Cell ID	Substrat	Cell no.	Voc [V]	Isc [mA/cm2]	FF	VocFF	Rsc [Ω cm2]		Isc (EQE)	Eff [%]
Oa111020dil1-2	Z2(40)	5	0.96	12.602	0.666	0.639	2424.342		11.62	7.43
	Z2(15)	1	0.95	14.65	0.661	0.628	2182.243		13.04	8.19
	Z2(4)	5	0.943	16.936	0.688	0.649	2428.593		14.09	9.14
	Z1	1	0.946	16.134	0.683	0.646	2303.072		14.3	9.24
degraded	Z2(40)	5	0.893	11.051	0.482	0.430	419.556		9.62	4.14
	Z2(15)	1	0.9	13.016	0.487	0.438	484.48		11.93	5.23
	Z2(4)	5	0.891	15.124	0.497	0.443	477.436		12.84	5.69
	Z1	1	0.884	14.44	0.5	0.442	487.848		12.95	5.72
Oa111021dil1-8	Z2(40)	16	0.954	11.176	0.664	0.633	1382.594		11.37	7.20
	Z2(15)	5	0.952	13.586	0.693	0.660	1171.53		12.53	8.27
	Z2(4)	13	0.923	14.54	0.698	0.644	1273.982		13.43	8.65
	Z1	5	0.898	15.537	0.661	0.594	1199.938		13.52	8.03
degraded	Z2(40)	16	0.919	10.464	0.627	0.576	1149.508		10.65	6.14
	Z2(15)	5	0.927	12.688	0.641	0.594	996.387		11.81	7.02
	Z2(4)	13	0.909	13.516	0.637	0.579	1022.495		12.65	7.32
	Z1	5	0.901	14.33	0.605	0.545	775.403		12.67	6.91
Oa111021dil1-32	Z2(40)	14	0.916	10.289	0.385	0.353	202.863		9.77	3.45
	Z2(15)	13	0.921	10.705	0.433	0.399	232.764		10.3	4.11
	Z2(4)	15	0.917	10.153	0.463	0.425	179.814		10.17	4.32
	Z1	2	0.885	10.338	0.458	0.405	181.138		8.84	3.58
degraded	Z2(40)	14	0.88	8.714	0.377	0.332	110.383		7.88	2.61
	Z2(15)	13	0.897	9.247	0.407	0.365	145.916		9.04	3.30
	Z2(4)	12	0.89	8.84	0.421	0.375	142.338		8.62	3.23
	Z1	2	0.86	8.682	0.406	0.349	186.453		7.95	2.78
Oa111021dil1-16b	Z2(40)	6	0.907	7.909	0.52	0.472	497.471		10.56	4.98
	Z2(15)	6	0.962	13.63	0.606	0.583	1061.167		12.1	7.05
	Z2(4)	15	0.939	14.773	0.592	0.556	1122.737		12.8	7.12
	Z1	15	0.861	14.679	0.537	0.462	606.635		12.56	5.81
degraded	Z2(40)	2	0.954	10.678	0.556	0.530	1042.626		9.85	5.22
	Z2(15)	13	0.963	13.14	0.581	0.560	1044.328		11.46	6.41
	Z2(4)	15	0.936	13.76	0.547	0.512	732.006		11.91	6.10
	Z1	15	0.857	13.46	0.461	0.395	397.418		11.6	4.58
Oa111024dil1-4b	Z2(40)	10	0.947	13.145	0.589	0.558	1479.893		11.56	6.45
	Z2(15)	16	0.935	14.272	0.583	0.545	1675.866		13.33	7.27
	Z2(4)	15	0.929	15.849	0.624	0.580	1769.269		14.19	8.23
	Z1	14	0.884	16.586	0.624	0.552	827.761		14.19	7.83
degraded	Z2(40)	10	0.902	12.19	0.509	0.459	899.692		11.02	5.06
	Z2(15)	16	0.9	13.291	0.51	0.459	714.135		12.57	5.77
	Z2(4)	15	0.904	14.798	0.539	0.487	809.906		13.38	6.52
	Z1	14	0.875	15.317	0.524	0.459	565.862		13.4	6.14
Oa111024dil1-1b	Z2(40)	3	0.524	11.149	0.504	0.264	350.772		9.37	2.47
	Z2(15)	15	0.504	13.544	0.52	0.262	284.103		12.08	3.17
	Z2(4)	2	0.495	13.867	0.536	0.265	350.006		13.04	3.46
	Z1	6	0.478	15.509	0.532	0.254	371.405		7.32	1.86
degraded	Z2(40)	7	0.565	9.073	0.361	0.204	154.801		7.28	1.48
	Z2(15)	15	0.535	10.473	0.367	0.196	138.489		9.11	1.79
	Z2(4)	2	0.548	11.19	0.369	0.202	151.836		10.36	2.09
	Z1	6	0.532	12.67	0.378	0.201	139.596		11.09	2.23
Oa111031dil1-1	Z2(40)	8	0.637	10.731	0.619	0.394	552.938		11.77	4.64
	Z2(15)	6	0.59	14.22	0.684	0.404	543.497		13.77	5.56
	Z2(4)	13	0.65	15.937	0.68	0.442	643.251		15.04	6.65
	Z1	16	0.533	16.719	0.654	0.349	413.796		15.05	5.25
degraded	Z2(40)	8	0.593	10.173	0.534	0.317	565.734		11.1	3.51
	Z2(15)	6	0.54	13.41	0.56	0.302	426.046		13.07	3.95
	Z2(4)	9	0.602	15.361	0.576	0.347	482.966		14.18	4.92
	Z1	16	0.526	15.451	0.535	0.281	293.764		14.05	3.95
Oa111101dil1-4	Z2(40)	6	0.933	12.946	0.692	0.646	2487.498		12.06	7.79
	Z2(15)	7	0.936	14.765	0.697	0.652	3104.789		13.92	9.08
	Z2(4)	1	0.922	15.919	0.717	0.661	3626.806		14.84	9.81
	Z1	7	0.891	16.23	0.708	0.631	2539.109		15.04	9.49
degraded	Z2(40)	6	0.9	12.095	0.607	0.546	1184.317		11.79	6.44
	Z2(15)	7	0.899	13.98	0.613	0.551	1024.579		13.31	7.33
	Z2(4)	1	0.89	15.094	0.606	0.539	896.091		14.24	7.68
	Z1	7	0.868	15.259	0.591	0.513	828.477		14.31	7.34

Cell ID	Substrat	Cell no.	Voc [V]	Isc [mA/cm2]	FF	VocFF	Rsc [Ω cm2]	Isc (EQE)	Eff [%]
Oa111101dil1-16	Z2(40)	3	0.964	10.595	0.633	0.610	1113.193	10.42	6.36
	Z2(15)	4	0.96	12.77	0.693	0.665	1886.977	12.46	8.29
	Z2(4)	6	0.938	15.095	0.717	0.673	1875.213	13.21	8.88
	Z1	13	0.919	13.784	0.686	0.630	1400.856	13.11	8.26
degraded	Z2(40)	5	0.938	9.869	0.607	0.569	1359.819	10.25	5.84
	Z2(15)	1	0.941	11.9	0.612	0.576	1152.605	11.89	6.85
	Z2(4)	6	0.916	14.225	0.627	0.574	916.152	12.52	7.19
	Z1	5	0.898	12.963	0.589	0.529	764.159	12.35	6.53
Oa111101dil1-64	Z2(40)	4	0.861	9.297	0.191	0.164	143.969	10.12	1.66
	Z2(15)	13	0.852	11.337	0.186	0.158	110.453	12.1	1.92
	Z2(4)	13	0.845	11.085	0.214	0.181	51.538	9.29	1.68
	Z1	4	0.843	9.037	0.294	0.248	48.832	8.22	2.04
degraded	Z2(40)	8	0.823	3.716	0.362	0.298	100.969	3.3	0.98
	Z2(15)	13	0.823	4.858	0.308	0.253	61.17	4.86	1.23
	Z2(4)	1	0.812	5.274	0.309	0.251	63.74	4.8	1.20
	Z1	4	0.805	5.044	0.34	0.274	102.242	4.56	1.25
Oa111102dil1-2	Z2(40)	6	0.944	12.002	0.653	0.616	2724.545	12	7.40
	Z2(15)	8	0.947	14.203	0.658	0.623	2113.55	13.6	8.47
	Z2(4)	7	0.943	15.609	0.687	0.648	2387.182	14.54	9.42
	Z1	5	0.935	15.452	0.697	0.652	2569.99	14.65	9.55
degraded	Z2(40)	6	0.892	11.436	0.514	0.458	950.998	11.4	5.23
	Z2(15)	8	0.894	13.149	0.523	0.468	712.857	12.77	5.97
	Z2(4)	7	0.886	14.559	0.51	0.452	786.514	13.62	6.15
	Z1	5	0.877	14.281	0.514	0.451	732.251	13.68	6.17
Oa111102dil1-8	Z2(40)	8	0.631	11.178	0.721	0.455	1458.786	11.5	5.23
	Z2(15)	13	0.604	14.074	0.695	0.420	635.479	12.98	5.45
	Z2(4)	13	0.63	14.422	0.701	0.442	916.047	14.05	6.20
	Z1	16	0.582	15.212	0.648	0.377	544.836	14.14	5.33
degraded	Z2(40)	8	0.616	10.472	0.636	0.392	948.103	10.87	4.26
	Z2(15)	13	0.594	13.209	0.624	0.371	582.12	12.68	4.70
	Z2(4)	13	0.648	13.597	0.627	0.406	694.454	13.38	5.44
	Z1	16	0.585	14.107	0.562	0.329	381.483	13.24	4.35
Oa111102dil1-32	Z2(40)	2	0.643	10.485	0.567	0.365	788.304	2.47	0.90
	Z2(15)	15	0.96	11.413	0.608	0.584	905.644	11.28	6.58
	Z2(4)	5	0.945	12.761	0.647	0.611	891.79	11.89	7.27
	Z1	4	0.922	12.979	0.612	0.564	632.275	11.79	6.65
degraded	Z2(40)	15	0.944	9.607	0.546	0.515	610.392	9.24	4.76
	Z2(15)	1	0.933	10.754	0.541	0.505	563.866	10.53	5.32
	Z2(4)	4	0.914	11.651	0.555	0.507	582.938	10.18	5.16
	Z1	4	0.897	11.739	0.517	0.464	458	11.06	5.13
Oa111107	Z2(40)	12	0.96	10.82	0.482	0.463	166.046	9.63	4.46
	Z2(15)	13	0.959	11.034	0.505	0.484	173.372	10.26	4.97
	Z2(4)	1	0.935	11.909	0.529	0.495	219.199	10.6	5.24
	Z1	16	0.914	12.108	0.548	0.501	160.758	10.92	5.47
degraded	Z2(40)	12	0.898	9.213	0.453	0.407	348.939	8.19	3.33
	Z2(15)	14	0.902	9.549	0.472	0.426	342.023	8.36	3.56
	Z2(4)	1	0.891	10.026	0.472	0.421	338.599	8.92	3.75
	Z1	16	0.869	9.827	0.468	0.407	271.796	8.71	3.54
Oa111109dil1-1	Z2(40)	8	0.941	11.404	0.705	0.663	2067.98	11.94	7.92
	Z2(15)	1	0.95	13.771	0.682	0.648	2380.834	13.99	9.06
	Z2(4)	8	0.943	15.883	0.713	0.672	2441.128	14.9	10.02
	Z1	1	0.938	16.657	0.708	0.664	2437.604	15.19	10.09
degraded	Z2(40)	16	0.884	10.422	0.591	0.522	1009.592	10.97	5.73
	Z2(15)	15	0.883	13.76	0.592	0.523	908.495	13.19	6.89
	Z2(4)	8	0.879	14.96	0.58	0.510	848.504	13.98	7.13
	Z1	1	0.872	15.513	0.572	0.499	771.104	14.21	7.09
Oa111109dil1-8	Z2(40)	9	0.958	11.437	0.619	0.593	1194.398	11.53	6.84
	Z2(15)	11	0.243	13.734	0.67	0.163	1761.772	13.32	2.17
	Z2(4)	13	0.964	14.804	0.704	0.679	1706.53	14.01	9.51
	Z1	1	0.955	14.182	0.693	0.662	1450.728	14	9.27
degraded	Z2(40)	10	0.929	10.866	0.571	0.530	1201.398	11.13	5.90
	Z2(15)	14	0.934	14.019	0.579	0.541	1102.305	11.98	6.48
	Z2(4)	13	0.916	13.806	0.57	0.522	1042.022	13.15	6.87
	Z1	7	0.899	13.701	0.544	0.489	864.271	13.15	6.43

Cell ID	Substrat	Cell no.	Voc [V]	Isc [mA/cm2]	FF	VocFF	Rsc [Ω cm2]		Isc (EQE)	Eff [%]
Oa111121b	Z2(40)	13	0.777	10.276	0.232	0.180	810.305		10.68	1.93
	Z2(15)	13	0.788	11.916	0.236	0.186	439.322		11.95	2.22
	Z2(4)	13	0.817	11.891	0.303	0.248	158.306		11.87	2.94
	Z1	13	0.802	11.524	0.329	0.264	14.686		7.04	1.86
Oa111122	Z2(40)	13	0.769	9.43	0.224	0.172	537.836		10.73	1.85
	Z2(15)	13	0.615	12.262	0.271	0.167	213.55		12.7	2.12
	Z2(4)	8	0.809	14.075	0.239	0.193	211.476		12.17	2.35
	Z1	4	0.829	12.672	0.312	0.259	152.585		12.38	3.20
Oa111125dil1-48	Z2(40)	4	0.822	9.456	0.203	0.167	297.265		9.79	1.63
	Z2(15)	13	0.825	12.247	0.203	0.167	107.032		12.33	2.06
	Z2(4)	16	0.827	11.847	0.267	0.221	92.532		11.2	2.47
	Z1	13	0.8	10.374	0.319	0.255	58.69		9.34	2.38
degraded	Z2(40)	4	0.813	6.556	0.24	0.195	51.752		6.81	1.33
	Z2(15)	13	0.812	8.973	0.229	0.186	40.773		9	1.67
	Z2(4)	16	0.813	8.767	0.292	0.237	53.664		8.22	1.95
	Z1	13	0.797	7.622	0.345	0.275	64.234		6.71	1.85
Oa111125dil1-16	Z2(40)	16	0.942	13.854	0.604	0.569	595.759		12.97	7.38
	Z2(15)	1	0.938	15.305	0.573	0.537	524.096		14.66	7.88
	Z2(4)	13	0.912	15.182	0.656	0.598	687.859		14.5	8.67
	Z1	8	0.895	16.491	0.631	0.565	676.69		15.25	8.61
degraded	Z2(40)	16	0.919	11.84	0.565	0.519	525.735		10.71	5.56
	Z2(15)	1	0.923	12.438	0.554	0.511	494.739		11.69	5.98
	Z2(4)	13	0.903	12.887	0.571	0.516	524.646		12.06	6.22
	Z1	8	0.886	13.37	0.492	0.436	339.832		11.63	5.07
Oa111128th600	Z2(40)	10	0.667	14.215	0.352	0.235	111.78		10.12	2.38
	Z2(15)	13	0.946	15.504	0.637	0.603	1544.696		14.24	8.58
	Z2(4)	13	0.926	17.274	0.672	0.622	1496.61		14.92	9.28
	Z1	1	0.916	16.809	0.677	0.620	1664.98		14.11	8.75
degraded	Z2(40)	10	0.422	12.605	0.301	0.127	48.812		9.45	1.20
	Z2(15)	13	0.926	13.729	0.558	0.517	495.774		12.81	6.62
	Z2(4)	13	0.912	15.427	0.565	0.515	509.162		13.28	6.84
	Z1	1	0.905	14.492	0.527	0.477	449.161		12.43	5.93
Oa111128th100	Z2(40)	1	0.975	9.319	0.758	0.739	2479.328		9.43	6.97
	Z2(15)	13	0.969	10.593	0.754	0.731	1948.814		10.5	7.67
	Z2(4)	5	0.947	9.73	0.746	0.706	1740.506		11.07	7.82
	Z1	13	0.902	11.522	0.709	0.640	1264.75		11.14	7.12
degraded	Z2(40)	1	0.932	8.739	0.699	0.651	1494.89		8.74	5.69
	Z2(15)	13	0.933	9.97	0.696	0.649	1510.23		9.79	6.36
	Z2(4)	5	0.918	9.03	0.69	0.633	1760.467		10.35	6.56
	Z1	13	0.884	10.684	0.642	0.568	1011.779		10.37	5.89
Oa111129th300	Z2(40)	13	0.96	12.333	0.63	0.605	1562.208		12.35	7.47
	Z2(15)	14	0.96	14.488	0.689	0.661	2055.46		13.41	8.87
	Z2(4)	1	0.942	16.001	0.708	0.667	1309.203		14.1	9.40
	Z1	4	0.918	14.252	0.702	0.644	1817.959		13.8	8.89
degraded	Z2(40)	13	0.931	11.521	0.572	0.533	774.582		11.52	6.13
	Z2(15)	14	0.94	13.636	0.615	0.578	811.466		12.65	7.31
	Z2(4)	1	0.925	14.864	0.624	0.577	853.352		13.24	7.64
	Z1	12	0.897	13.873	0.626	0.562	867.363		12.57	7.06
Oa111129Ti160	Z2(40)	5	0.971	11.368	0.73	0.709	2226.669		10.96	7.77
	Z2(15)	9	0.97	13.3	0.735	0.713	2566.769		12.54	8.94
	Z2(4)	5	0.957	14.63	0.747	0.715	2114.084		13.3	9.51
	Z1	5	0.931	14.779	0.723	0.673	1532.204		13.21	8.89
degraded	Z2(40)	5	0.942	10.864	0.657	0.619	1988.102		10.41	6.44
	Z2(15)	13	0.942	12.598	0.672	0.633	1184.82		11.97	7.58
	Z2(4)	5	0.931	13.803	0.666	0.620	1086.147		12.56	7.79
	Z1	5	0.914	13.833	0.621	0.568	938.823		12.29	6.98
Oa111129Tp160	Z2(40)	5	0.969	10.883	0.654	0.634	1831.293		11.03	6.99
	Z2(15)	13	0.974	13.253	0.686	0.668	1903.829		12.26	8.19
	Z2(4)	14	0.948	15.057	0.71	0.673	1374.087		13.5	9.09
	Z1	5	0.926	14.268	0.694	0.643	1665.513		13.17	8.46
degraded	Z2(40)	5	0.929	10.216	0.585	0.543	1046.867		10.31	5.60
	Z2(15)	13	0.939	12.426	0.614	0.577	1003.849		11.96	6.90
	Z2(4)	14	0.919	14.144	0.617	0.567	853.829		12.66	7.18
	Z1	5	0.898	13.211	0.587	0.527	758.534		12.13	6.39

Cell ID	Substrat	Cell no.	Voc [V]	Isc [mA/cm2]	FF	VocFF	Rsc [Ω cm2]		Isc (EQE)	Eff [%]
Oa111201th70a	Z2(40)	6	0.908	11.156	0.721	0.655	2244.296		10.93	7.16
	Z2(15)	6	0.914	12.936	0.73	0.667	2517.689		12.48	8.33
	Z2(4)	15	0.91	14.05	0.737	0.671	1623.911		13.25	8.89
	Z1	5	0.908	14.479	0.726	0.659	1312.094		13.06	8.61
Oa111201th70b	Z2(40)	1	0.974	8.235	0.741	0.722	3486.624		8.21	5.93
	Z2(15)	3	0.97	9.484	0.739	0.717	1735.125		9.53	6.83
	Z2(4)	13	0.953	10.798	0.743	0.708	2033.981		10.44	7.39
	Z1	5	0.914	11.255	0.701	0.641	1240.135		10.57	6.77
degraded	Z2(40)	1	0.929	7.767	0.679	0.631	1539.335		7.64	4.82
	Z2(15)	16	0.922	8.941	0.678	0.625	1151.591		8.9	5.56
	Z2(4)	13	0.914	9.991	0.679	0.621	1068.72		9.67	6.00
	Z1	1	0.89	10.533	0.64	0.570	833.712		9.89	5.63
Oa111202dil1-64	Z2(40)	13	0.815	10.66			461.976		11.25	
	Z2(15)	13	0.782	12.487	0.212	0.166	529.167		12.61	2.09
	Z2(4)	13	0.801	13.001	0.217	0.174	130.457		12.49	2.17
	Z1	13	0.747	11.447	0.261	0.195	70.073		9.98	1.95
degraded	Z2(40)	13	0.809	6.7	0.24	0.194	41.162		6.22	1.21
	Z2(15)	13	0.782	9.553	0.18	0.141	40.031		9.07	1.28
	Z2(4)	13	0.793	9.82	0.226	0.179	41.489		8.91	1.60
	Z1	13	0.757	8.425	0.286	0.217	48.902		7.23	1.57
Oa111202Tp+i160	Z2(40)	8	0.977	11.659	0.651	0.636	2382.013		10.91	6.94
	Z2(15)	4	0.984	12.467	0.666	0.655	2108.457		12.19	7.99
	Z2(4)	2	0.971	13.867	0.708	0.687	1753.555		12.83	8.82
	Z1	8	0.943	13.992	0.696	0.656	1577.042		12.76	8.37
degraded	Z2(40)	8	0.944	10.941	0.585	0.552	1059.147		10.45	5.77
	Z2(15)	4	0.951	11.648	0.596	0.567	1213.21		11.49	6.51
	Z2(4)	2	0.944	12.985	0.62	0.585	1086.404		12.12	7.09
	Z1	8	0.922	13.077	0.593	0.547	860.443		11.97	6.54
Oa111202Ti160th100	Z2(40)	15	0.962	5.579	0.717	0.690	11.98		8.86	6.11
	Z2(15)	5	0.973	10.89	0.733	0.713	1611.31		10.47	7.47
	Z2(4)	5	0.964	11.646	0.746	0.719	1305.811		11.08	7.97
	Z1	5	0.935	12.104	0.706	0.660	1592.449		11.11	7.33
degraded	Z2(40)	15	0.932	5.247	0.656	0.611	2063.06		8.37	5.12
	Z2(15)	5	0.943	10.212	0.67	0.632	1288.573		9.82	6.20
	Z2(4)	5	0.936	10.955	0.674	0.631	1084.849		10.4	6.56
	Z1	5	0.913	11.202	0.641	0.585	998.594		10.42	6.10

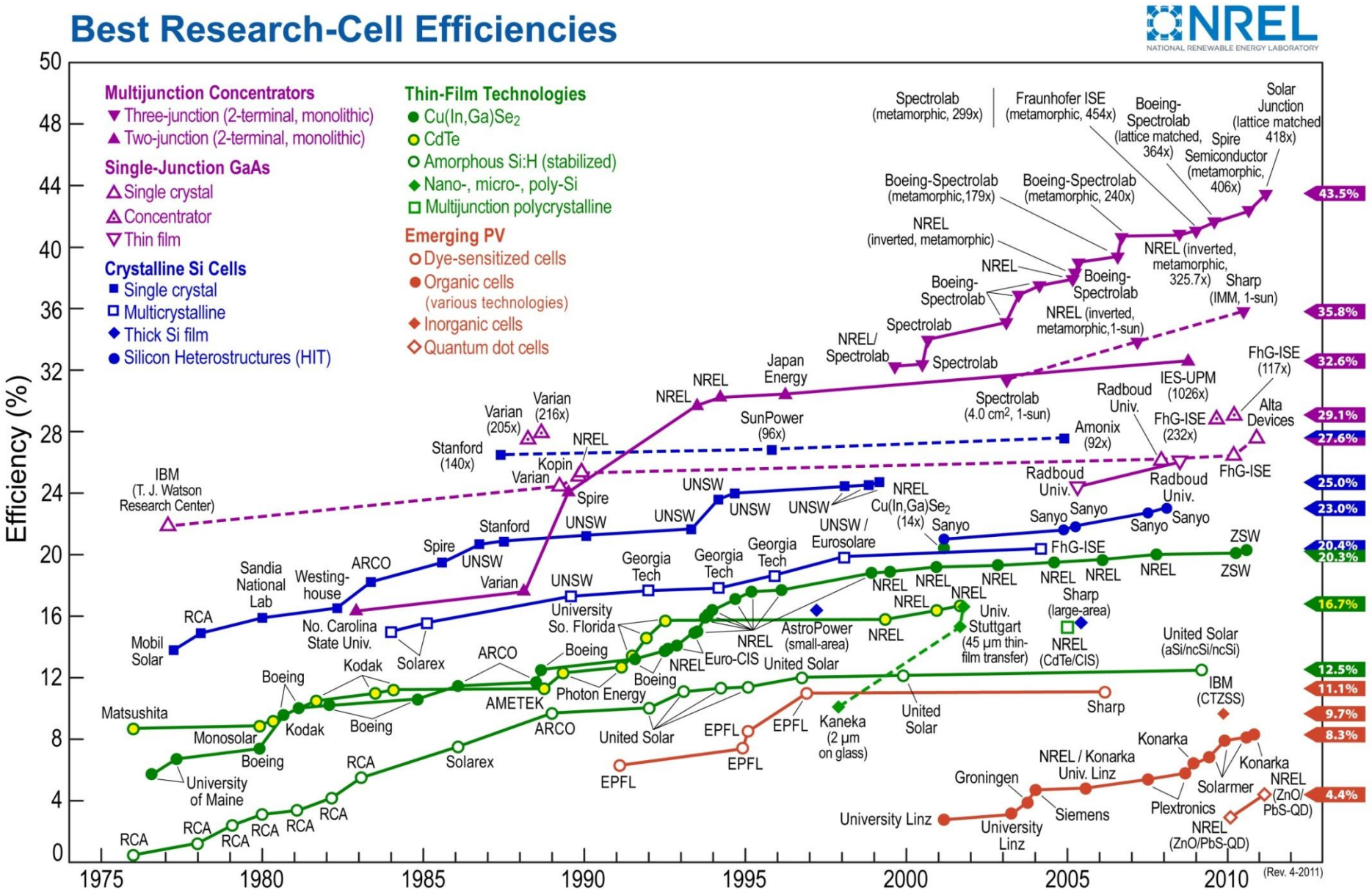
Best Research-Cell Efficiencies
NREL
NATIONAL RENEWABLE ENERGY LABORATORY
Multijunction Concentrators
Three-junction (2-terminal, monolithic)
Two-junction (2-terminal, monolithic)
Single-Junction GaAs
Single crystal
Concentrator
Thin film
Crystalline Si Cells
Single crystal
Multicrystalline
Thick Si film
Silicon Heterostructures (HIT)
Thin-Film Technologies
Cu(In,Ga)Se2
CdTe
Amorphous Si:H (stabilized)
Nano-, micro-, poly-Si
Multijunction polycrystalline
Emerging PV
Dye-sensitized cells
Organic cells
(various technologies)
Inorganic cells
Quantum dot cells
Efficiency (%)
0
4
8
12
16
20
24
28
32
36
40
44
48
50
1975
1980
1985
1990
1995
2000
2005
2010
(Rev. 4-2011)
43.5%
35.8%
32.6%
29.1%
27.6%
25.0%
23.0%
20.4%
20.3%
16.7%
12.5%
11.1%
9.7%
8.3%
4.4%
Spectrolab (metamorphic, 299x)
Fraunhofer ISE (metamorphic, 454x)
Boeing-Spectrolab (lattice matched, 364x)
Spire Semiconductor (metamorphic, 406x)
Solar Junction (lattice matched 418x)
Boeing-Spectrolab (metamorphic,179x)
Boeing-Spectrolab (metamorphic, 240x)
NREL (inverted, metamorphic)
NREL (inverted, metamorphic, 325.7x)
Sharp (IMM, 1-sun)
NREL
Boeing-Spectrolab
NREL (inverted, metamorphic,1-sun)
NREL/ Spectrolab
Spectrolab
Spectrolab (4.0 cm2, 1-sun)
FhG-ISE (117x)
Radboud Univ.
IES-UPM (1026x)
Alta Devices
FhG-ISE (232x)
Amonix (92x)
FhG-ISE
Radboud Univ.
Radboud Univ.
Japan Energy
NREL
NREL
SunPower (96x)
Varian (205x)
Varian (216x)
Stanford (140x)
NREL
Kopin
Varian
Spire
IBM (T. J. Watson Research Center)
UNSW
UNSW
UNSW
UNSW
UNSW
NREL Cu(In,Ga)Se2 (14x)
Sanyo
Sanyo
Sanyo
Sanyo
Sanyo
Stanford
UNSW
UNSW / Eurosolare
FhG-ISE
ZSW
ZSW
Spire
UNSW
Georgia Tech
Georgia Tech
Georgia Tech
Sandia National Lab
Westing-house
ARCO
Varian
UNSW
NREL
NREL
NREL
NREL
NREL
NREL
NREL
NREL
Sharp (large-area)
RCA
University So. Florida
Univ. Stuttgart (45 µm thin-film transfer)
Mobil Solar
No. Carolina State Univ.
Solarex
NREL
AstroPower (small-area)
NREL
NREL (CdTe/CIS)
United Solar (aSi/ncSi/ncSi)
ARCO
Boeing
Kodak
Euro-CIS
United Solar
Boeing
Boeing
Photon Energy
IBM (CTZSS)
Matsushita
AMETEK
Sharp
Monosolar
Kodak
Boeing
ARCO
United Solar
EPFL
EPFL
Kaneka (2 µm on glass)
United Solar
Boeing
Konarka
NREL / Konarka Univ. Linz
Konarka
Groningen
Solarmer
NREL (ZnO/ PbS-QD)
University of Maine
RCA
Solarex
Plextronics
Siemens
University Linz
University Linz
NREL (ZnO/PbS-QD)
RCA
RCA
RCA
RCA
RCA
RCA
EPFL